Oxidation Rates and Redox Stabilization of Ferrous Iron in Trioctahedral Smectites

Robert J. Kupper[1], Nanqing Zhou[2], Clara S. Chan[2,3], Aaron Thompson[4], Jeffrey G. Catalano[1,5*]

1. Department of Earth and Planetary Sciences, Washington University, Saint Louis, MO 63130, USA
2. School of Marine Science and Policy, University of Delaware, Newark, DE 19716, USA
3. Department of Earth Sciences, University of Delaware, Newark, DE 19716, USA
4. Department of Crop and Soil Science, University of Georgia, Athens, GA 30602, USA
5. McDonnell Center for the Space Sciences, Washington University, Saint Louis, MO 63130, USA

*Corresponding author: catalano@wustl.edu

Submitted to *Geochimica et Cosmochimica Acta*
December 2022
Revised June 2023

ABSTRACT

Iron(II)-bearing trioctahedral smectites (saponites) form during anoxic alteration of basaltic rock. They are predicted to have been widespread on the early Earth and are observed in the oceanic subsurface today. Smectite structures, including the occupancy of sites in the octahedral sheet, affect iron redox behavior but the rates and products of trioctahedral smectite oxidation have been largely unexplored to date. In this study we synthesized two Fe(II)-bearing trioctahedral smectites, one moderate (22 wt. % Fe) and one high (27 wt. % Fe) in iron content. We then examined the rate, extent, and products of their oxidation by dissolved oxygen, nitrite, and hydrogen peroxide. Dissolved oxygen caused partial oxidation of Fe(II) in the smectites with 14 to 43% of Fe(II) unoxidized after 20 to 30 days of exposure. The rate and extent of oxidation correlated with the dissolved oxygen concentration and the Fe(II) content of the clay. The incomplete oxidation in these experiments is consistent with the mixed-valent trioctahedral smectites observed in oxidized natural samples but contrasts with the complete reoxidation by oxygen shown by chemically- or microbially-reduced dioctahedral smectites. Oxidation of structural Fe(II) by 5 mmol L^{-1} nitrite was negligible for the moderate-iron smectite and yielded only ~17% oxidation after 54 days of reaction for the high-iron smectite. Hydrogen peroxide caused rapid and near-complete oxidation of both clays. Powder X-ray diffraction, variable-temperature Mössbauer spectroscopy, and extended X-ray absorption fine structure spectroscopy together detected no crystalline or short-range-ordered secondary phases and show that oxidized iron remained in the trioctahedral smectite structure. The recalcitrant Fe(II) pool in oxidized trioctahedral smectites exists in less distorted sites than Fe(II) in the initial clays. Its unreactive nature at prolonged reaction times indicates an elevated redox potential generated by the local coordination environment. Slower oxidation rates create a larger recalcitrant Fe(II) pool,

suggesting kinetic competition between oxidation and a process involved in redox stabilization, such as electron exchange between octahedral iron sites or deprotonation of hydroxyl groups in the structure. The resistance to complete oxidation of trioctahedral ferrous smectites and their full retention of iron demonstrates that transitions from anoxic to oxic conditions generate mixed-valence smectites rather than a mixture of new phases. Identifying the diagenetic products of mixed-valent trioctahedral smectites may provide an indicator in the rock record of past redox cycling. Substantial portions of structural Fe(II) in trioctahedral smectites display slow abiotic oxidation kinetics and represent potential electron donors for both microaerophilic iron oxidizing and nitrate-reducing, iron-oxidizing microorganisms in altered mafic rocks and related settings.

Keywords: Iron Redox; Oxidation Rate; Trioctahedral Smectite; Mössbauer Spectroscopy

1. INTRODUCTION

Aqueous alteration of basalts produces Mg- and Fe-rich smectites (Velde and Meunier, 2008). Under anoxic conditions, these minerals incorporate ferrous iron and are predominantly trioctahedral saponite smectites (Alt et al., 1986; Andrews, 1980; Badaut et al., 1985; Kohyama et al., 1973). There are numerous occurrences of Fe(II)-bearing smectites (primarily saponites) in the anoxic subsurface of the oceanic crust as vesicle and fracture infilling and alteration crusts (Alt, 1999; Andrews, 1980; Teagle et al., 1996). Similarly Fe(II) smectites form authigenically in anoxic sediments affected by hydrothermal input in the Atlantis II basin in the Red Sea (Badaut et al., 1985). Analogous terrestrial locations contain Fe(II)-bearing trioctahedral smectites in the Deccan Traps flood basalts (Parthasarathy et al., 2003) and low temperature hydrothermal systems in Iceland (Kristmannsdottir, 1979). Despite its overall composition, the glassy, rhyolitic Oya tuff contains both high-iron trioctahedral and low-iron dioctahedral ferrous smectites (Kohyama et al., 1973) formed from altered mineral fragments. Trioctahedral ferrous smectites are also found intercalated with vermiculite in immature orogenic sediments as a result of alteration of biotite and chlorite (Craw et al., 1995). Subsequent oxidation of these clay minerals in the upper oceanic crust (Alt, 1999; Alt et al., 1986) and in exposed terrestrial environments (Craw et al., 1995; Kohyama et al., 1973) produces Fe(III)-bearing phyllosilicate and oxide minerals.

Trioctahedral smectites likely retained a predominantly ferrous state before the oxygenation of Earth's atmosphere in the Paleoproterozoic (Lyons et al., 2014) possibly persisting as a dominant marine clay until the deep ocean oxygenated in the Neoproterozoic (Canfield et al., 2007; Shen et al., 2002). The size of this smectite Fe(II) pool on the early Earth can be estimated based on current oceanic crust compositions and alteration depths and extents

(Alt, 1999; Alt et al., 1986). Assuming an area of oceanic crust equal to the modern ocean surface (3.62×10^8 km^2), a depth of crustal alteration of 500 m, a basaltic composition with 9 wt.% FeO_T and Fe(II)/Fe(Total) of 0.84, and 5% total alteration, we estimate that there was 1.9×10^{19} moles of Fe(II) in smectites and related phyllosilicates in the shallow oceanic crystal of the early Earth. If the ocean prior to the Great Oxidation Event (GOE) contained ~0.1 mmol L^{-1} dissolved Fe(II) (Holland, 2004) then it hosted 1.3×10^{17} moles of Fe(II), assuming as a first approximation a total volume equal to today. These coarse estimates yield a total Fe(II) content of the altered oceanic crust more than 200 times that of dissolved Fe(II) in pre-GOE seawater. Recent geochemical modeling (Hao et al., 2017) and examination of Archean paleosols (Babechuk et al., 2019) suggest that ferrous smectites were present on land and in Archean lacustrine systems in addition to marine settings. Similar clays, possibly as mixed valent phases, also occur in lacustrine mudstones at Gale Crater on Mars (Treiman et al., 2014; Vaniman et al., 2014). Iron-rich smectites may also occur on the surface of Ceres (Ehlmann et al., 2018; Rivkin et al., 2006) and on icy worlds with subsurface oceans (Neveu et al., 2017). Trioctahedral smectites thus represent a large Fe(II) pool on the early Earth that may also occur on potentially habitable bodies in the Solar System.

Despite widespread occurrence in anoxic aquatic environments, trioctahedral ferrous smectites are rarely studied because of the difficulty in obtaining, storing, and purifying samples without causing oxidation (Alt et al., 1986; Andrews et al., 1983; Badaut et al., 1985; Craw et al., 1995). Upon exposure to oxygen, iron in these smectites partially oxidizes (Chemtob et al., 2017; Kohyama et al., 1973) yielding a mixed valent phase similar in composition to well-studied saponite smectite from Griffith Park, California (Treiman et al., 2014). To gain further insight into these clay minerals, studies have investigated synthetic trioctahedral ferrous smectites,

characterizing their formation mechanisms (Baldermann et al., 2014), composition, structure, and spectral properties (Chemtob et al., 2015; Fox et al., 2021; Sakuma et al., 2022), as well as oxidation products (Chemtob et al., 2017). Notably, a prior study (Chemtob et al., 2017) found that oxidation of ferrous iron in trioctahedral smectites by dissolved oxygen in air-equilibrated solutions was incomplete after 7 days, although hydrogen peroxide caused rapid and complete oxidation. Hydrothermal recrystallization of these fully-oxidized clays generated nanoparticulate hematite, but it is unclear whether iron was ejected from the clay structure to produce an iron oxide during oxidation or simply was more easily observed after the hydrothermal treatment because of conversion from ferrihydrite to hematite. The kinetics of iron oxidation in trioctahedral smectites, the extent of oxidation under different oxygen concentrations, and their reactivity with other potential oxidants remain unexamined to date.

In contrast, the redox chemistry of iron in nontronite and other dioctahedral smectites containing ferric iron has been studied extensively (Dong et al., 2022; Komadel et al., 1995; Pentráková et al., 2013; Stucki, 2011; Zhao et al., 2015), providing insight into potential behavior displayed by Fe(II)-bearing trioctahedral smectites. Reduction of dioctahedral smectites may be accompanied by iron migration through vacancies, forming trioctahedral domains (Drits and Manceau, 2000; Fialips et al., 2002b; Manceau et al., 2000a; Manceau et al., 2000b) analogous to trioctahedral ferrous smectites. However, this also creates excessive negative layer charge and may cause interlayer collapse (Dong et al., 2009; Khaled and Stucki, 1991; Shen and Stucki, 1994; Shen et al., 1992), features not displayed by trioctahedral smectites natively containing Fe(II). Oxidation of Fe(II) in reduced dioctahedral smectites is typically complete (Komadel et al., 1995; Shen and Stucki, 1994) and may displays two-stage kinetics (Neumann et al., 2008). As noted above, the oxidation rates of synthetic trioctahedral ferrous smectites have

not been studied so it is unclear if the incomplete oxidation previously observed (Chemtob et al., 2017) is a result of slow kinetics or a recalcitrant Fe(II) fraction not seen in reduced dioctahedral smectites. Two stage (re)oxidation kinetics for dioctahedral clays is attributed to redox interconversion between two distinct iron sites, possibly related to structural rearrangement in the octahedral sheet following oxidation (Neumann et al., 2008). While reoxidized dioctahedral smectites retain some trioctahedral clusters (Fialips et al., 2002a), the low vacancy content of trioctahedral sheets may preclude the structural changes associated with oxidation of dioctahedral smectites and thus yield distinct kinetic behavior.

Additional aspects of Fe(II) oxidation in smectites remain unresolved despite the extensive investigations of reduced dioctahedral clays. While studies have examined the reoxidation of several dioctahedral smectites in oxygen-equilibrated fluids (Fialips et al., 2002a; Komadel et al., 1990; Komadel et al., 1999), oxidation rates have not been examined under microoxic levels favored by microaerophilic iron oxidizers. Separately, the potential role of nitrite as an oxidant of Fe(II) in smectites is uncertain. Nitrite is a reactive intermediate formed by denitrifying bacteria (Betlach and Tiedje, 1981; Glass and Silverstein, 1998) and implicated in oxidation of dissolved Fe(II) (Klueglein and Kappler, 2013; Klueglein et al., 2014). Prior literature is contradictory regarding whether nitrite abiotically oxidizes structural Fe(II) in reduced dioctahedral smectites, with reports of both minor reactivity (Zhao et al., 2013) and substantial reactivity (Grabb et al., 2017) on timescales of ten to twenty days.

In this study, two trioctahedral ferrous smectites of different compositions were synthesized and their oxidation rates were determined in the presence of dissolved oxygen at atmospheric (21% O_2) and microoxic (2% O_2) levels. The observed rates were fitted to a kinetic model and then compared across different smectite compositions and oxygen concentrations to

explore how oxidation rates and extents vary with these parameters. The rates of oxidation of trioctahedral ferrous smectites with nitrite were also investigated. The products of each experiment were characterized by powder X-ray diffraction (XRD) to evaluate changes to the smectite unit cell and identify possible crystalline secondary phases. Mössbauer spectroscopy was utilized to analyze changes in iron speciation and detect potential secondary short-range-ordered (amorphous or nanocrystalline) iron phases. Extended X-ray absorption fine structure (EXAFS) spectroscopy evaluated changes in the local coordination environment of solid-phase iron following oxidation. Products of trioctahedral ferrous smectites exposed to hydrogen peroxide were also studied to assess structural alteration and the possible ejection of iron following near-complete oxidation of structural iron. Through these analyses, we constrain the oxidation behavior of trioctahedral ferrous smectites under exposure to oxidants relevant to both early Earth and modern subsurface environments.

2 MATERIALS AND METHODS

2.1. Synthesis of Trioctahedral Smectites

Two smectites were synthesized using a previously-published hydrothermal sol-gel method (Decarreau and Bonnin, 1986) modified to inhibit iron oxidation during heating (Chemtob et al., 2015). All synthesis steps that did not involve sealed vessels were carried out in an anaerobic chamber (Coy Laboratory Products, 96% N_2, 4% H_2, O_2 < 20 ppm). A secondary oxygen trap containing 40% potassium hydroxide and 10% pyrogallol was also employed in the anaerobic chamber. Water used in each step was ultrapure (>18.2 MΩ cm) and deoxygenated through sparging, first with nitrogen gas on the benchtop and then using the gas mix inside the anaerobic chamber. Dissolved oxygen concentrations were measured colorimetrically after

194 sparging (CHEMetrics test kit K-7540); all sparged waters contained undetectable dissolved
195 oxygen (detection limit of 2.5 μg L^{-1} , ~80 nmol L^{-1}). Synthesis began with formation of a gel by
196 combining a solution of sodium silicate with a mixture of aluminum, magnesium and iron(II)
197 chloride solutions at a ratio corresponding to a target final smectite composition (**Table 1**). After
198 aging for 24 hours, the gel and fluid were separated by centrifugation (50 mL Oak Ridge style
199 tubes with sealing caps, Beckman Coulter Avanti 30 centrifuge, F0850 rotor, 16500 rpm/29000
200 g), then resuspended in deoxygenated ultrapure water and centrifuged once more to remove any
201 excess salt. The washed gel was resuspended in water once more and adjusted to pH 9 with 0.5
202 mol L^{-1} sodium hydroxide or 1.0 mol L^{-1} hydrochloric acid. The gel suspension for each
203 synthesis was continuously-stirred and evenly divided in 10 mL increments into two, 200 mL
204 PTFE-lined, steel-jacketed hydrothermal vessels (Parr Instrument Company model 4748A)
205 which were sealed and transferred to a vacuum oven (Lindberg/BlueM V01218A). The oven was
206 evacuated and then backflushed with ultrahigh purity nitrogen gas five times and the sealed
207 vessels were then heated at 200°C for 15 days. The oven was set to a slight vacuum condition
208 (-30 kPa relative to atmospheric pressure) to maintain the door seal; the internal pressure did not
209 change over the 15-day heating period.
210 Following the hydrothermal treatment, the reactors were transferred back to the anaerobic
211 chamber and synthetic smectites were suspended in a 0.5 mol L^{-1} calcium chloride solution to
212 saturate the interlayer with calcium. After Ca-saturation the smectites suspensions were
213 centrifuged in sealed tubes (16500 rpm/29000 g) with the fluid then decanted. Excess dissolved
214 salts in the remaining liquid were removed by twice suspending the smectites were ultrapure
215 water and then centrifuging again in sealed tubes, with the supernatant decanted. The wet clay
216 pastes were transferred to a vacuum desiccator loaded with a 4 Å molecular sieve for drying. All

steps in the washing and drying process were carried out in the anaerobic chamber except for centrifugation. Once sufficiently dry, the samples were ground to a powder using an agate mortar and pestle and sealed in secondary containment within the anaerobic chamber to protect them from inadvertent oxidation.

2.2. Compositional Analysis of Synthetic Smectites

To determine the structural formula for each smectite, a lithium metaborate fusion (Amonette, 1994) method was used. 50 mg of smectite was finely ground in an agate mortar and pestle and combined with 350 mg of lithium metaborate flux in a graphite crucible. The mixture was then melted at 1050°C in a muffle furnace for fifteen minutes to produce a glass pellet which was quenched into 40 ml of 10% v./v. trace metal grade nitric acid in a centrifuge tube. This tube was then sealed and placed into a sonicating bath for 12 hours to ensure complete dissolution of the sample. The dissolved sample was diluted and measured on a Thermo Scientific iCap 7400 Duo inductively coupled plasma optical emission spectrometer (ICP-OES). The iron oxidation extent of the solids was determined colorimetrically using a modified 1,10-phenanthroline assay (Tarafder and Thakur, 2013). In place of the leaching procedure Tarafder and Thakur demonstrated for syenite and gabbro, recovered solids were completely dissolved by placing the sample into 10 ml of 20 g/l ammonium bifluoride solution. To ensure dissolution, samples were mixed continuously for 30 minutes in an end-over-end rotator. Following dissolution, 200 ul of the dissolved clay solution was added to two 2 ml cuvettes, one with 1200 ul of water and 200 ul of 5% hydroxylamine hydrochloride to reduce the ferric iron, and another with 1400 ul of water. 200 ul of 10% sodium citrate was then added to each sample to buffer the pH and finally 200 ul of 0.1% 1,10-phenanthroline was added to develop color in the presence of ferrous iron. These

cuvettes were then measured in a UV-Vis spectrometer to capture the absorbance at 510 nm. The elemental abundances obtained by ICP-OES were normalized to 22 anionic charges per half unit cell and cations were assigned to either tetrahedral, octahedral or interlayer sites according to their affinity with that site (Amonette, 1994). Iron was divided into ferrous and ferric pools based on the ratio obtained by colorimetry

2.3. Oxidation Kinetics Studies

Each kinetic study was conducted in an artificial freshwater media (Emerson and Floyd, 2005) for microaerophilic lithophiles that was chosen to replicate the conditions utilized in microbial cultures, e.g., (Zhou et al., 2022), and consistent with natural bicarbonate-buffered aquatic environments. The media contained 1 mL per liter each of ATCC Vitamin Supplement (ATCC MD-VS) and ATCC Trace Mineral Supplement (ATCC MD-TMS). Full media composition appears in **Table S1**; note that the 0.35 μmol L^{-1} Fe(II) in the media is <0.1% of the total Fe(II) in each experiment. A 10 mmol L^{-1} MES buffer was added to decrease the pH drift over the course of the experiment. For each replicate, 200 mg of smectite was suspended in 100 ml of the media and adjusted to an initial pH of 6.2±0.1 using 1 mol L^{-1} hydrochloric acid. This pH was chosen to mirror conditions used in microbial cultures, such as for the iron-oxidizing lithophile Sideroxydans lithotrophicus ES-1 (Emerson and Floyd, 2005), to enable comparisons with biotic studies (Zhou et al., 2022). Suspensions were kept in foil-wrapped 125 ml borosilicate serum bottles sealed with butyl rubber septa. Each experiment was conducted in triplicate.

In order to determine the rate of oxidation by dissolved oxygen, either air or a gas mixture of 78% N_2, 20% CO_2, and 2% O_2 was first humidified and then passed through a 0.22

μm filter membrane to each serum bottle at a rate of 50 mL min^{-1}. The gas mixture composition was selected to mirror the headspace used in microaerophilic microbial oxidation studies (Zhou et al., 2022). Suspensions were continuously stirred for the duration of the experiment. Temperature and dissolved oxygen were measured every 10 minutes for the duration of the experiments using a Pyro Science Firesting-O2 optode system with contactless sensor spots mounted on the inside walls of the serum bottles for oxygen, and a temperature probe in a separate smectite-free serum bottle.

Sodium nitrite was added to a second set of 125 mL serum bottles for both smectite compositions filled with 100 ml of media to a concentration of 5 mmol L^{-1}. Nitrite is a reactive intermediary produced during bacterial denitrification that has been shown to accumulate extracellularly (Betlach and Tiedje, 1981) up to mmol L^{-1} concentrations (Kappler et al., 2005; Weber et al., 2006). For both smectite compositions an oxidant-free control was also prepared. These serum bottles were then sealed inside the anaerobic chamber with butyl rubber stoppers. The control and nitrite experiments were kept on a horizontal orbital shaker table at 150 rpm and sampled inside the anaerobic chamber. Nitrite content was monitored using the Griess assay (Ivanov, 2004) on supernatant fluids collected at each time point. An analytical problem prevented nitrite quantification for the experiment with the high-iron smectite.

At each timepoint, a 3 mL subsample of the suspension was collected from each suspension and filtered onto a 0.22 μm PTFE filter membrane inside the anaerobic chamber. The filter was washed with deoxygenated ultrapure water to remove any adsorbed oxidants. Digestion in ammonium bifluoride solution followed by colorimetry was used to measure the extent of oxidation in the smectite sample collected via filtration at each timepoint; this method was identical to that used for the initial compositional analysis. At the end of each kinetic

experiment, the remaining smectite suspension in each reactor was centrifuged in sealed tubes (16500 rpm/29000 g) and then decanted to remove the reaction solution. The solids were resuspended once in ultrapure water followed again by centrifugation and decanting of the supernatant. The solids were then dried in a vacuum desiccator in the anaerobic chamber and then sealed in secondary containers until used for solid-phase analyses.

The rates of iron oxidation in the oxygen exposed smectites were quantified using a two-term second-order kinetic model whose rates are defined by Equation 1:

$$\frac{d[Fe(II)]}{dt} = k_1 {a_1}^2 + k_2 {a_2}^2 \quad \text{(Eq. 1)}$$

Where k_1 and k_2 are the two different rate constants that govern the portions of Fe(II) a_1 and a_2, respectively. The integrated form, with the additional non-reactive portion is given in Equation 2:

$$Fe(II)_t = \frac{a_1}{k_1 t(a_1+1)} + \frac{a_2}{k_2 t(a_2+1)} + a_3 \quad \text{(Eq. 2)}$$

$Fe(II)_t$ is the fraction of iron remaining as Fe(II) at time t and a_3 is the portion of Fe(II) that is recalcitrant to oxidation. Note that the sum of a_1, a_2, and a_3 represents the fitted Fe(II)/Fe(Total) at the start of the experiment (t = 0). These are not constrained to sum to 1 to enable simulation of a minor initial Fe(III) content, as seen for prior synthetic Fe(II)-bearing smectites (Chemtob et al., 2015; Fox et al., 2021). This integrated equation was fit to the data with parameters of the model determined in MATLAB using a Levenberg-Marquardt nonlinear least squares regression. Each datapoint was weighted by the experimental uncertainty in that point. The same model was applied to all datasets to enable the comparison of parameters between the studies. A two-term second-order model was chosen in line with previous published analysis of Fe(II) oxidation in smectites (Neumann et al., 2008). This prior work allowed for the interconversion of less reactive (k_1) to more reactive (k_2) sites, with a conversion rate determined through an oxidant

spike experiment. Our experiments maintained a continuous flow of oxygen and we did not determine an interconversion rate.

2.4. Oxidation by Hydrogen Peroxide

Both synthetic smectites were exposed to hydrogen peroxide in order to produce fully oxidized products. These experiments were not conducted in triplicate because oxidation was predicted to be complete and too rapid to be measured in kinetic studies. A suspension of 20 mg of smectite in 100 ml of media was prepared in a sealed 125 ml serum bottle for both compositions and stirred continuously with a magnetic stir bar. A 30% hydrogen peroxide solution was added at a ten to one molar ratio of H_2O_2 to Fe for each suspension, with a needle inserted to vent excess gas buildup. This process was carried out on the benchtop, not in an anaerobic chamber, because hydrogen peroxide decomposes to oxygen. Suspensions were vented and continuously stirred with a stir bar for 24 hours to allow for the decomposition of the remaining hydrogen peroxide before being transferred to the anaerobic chamber. Following oxidation, samples were filtered and stored similarly to other samples. The completion of oxidation was checked using the same colorimetric method to measure iron oxidation as with other samples.

2.5. Solid-phase Product Characterization

2.5.1. X-ray Diffraction

Powder XRD patterns for the synthesized smectites and reaction products were measured using Cu Kα radiation from an X-ray tube operating at 40 kV with a 40 mA current on a Bruker d8 Advance X-ray diffractometer equipped with a LYNXEYE XE energy-dispersive silicon strip

detector. Samples were evenly ground using an agate mortar and pestle and measured in a silicon zero-background sample holder. In order to prevent oxidation during measurement an acrylic dome was fitted over the samples to maintain an anoxic environment. Each sample was measured from 3˚ to 65˚ 2θ with 0.019° steps and 0.8 s integration time per step. By scanning over all 192 strips of the detector for 0.8 seconds each, a total integration time of 153.6 s is achieved for each 2θ position. Positions of the (001) peak and (06,33) *hk* band were determined by least-squares fitting utilizing a pseudo-Voigt profile and assuming a linear background.

2.5.2. Mössbauer Spectroscopy

Samples from one replicate in each set of experimental conditions were selected for Mössbauer analysis. These were evenly ground using an agate mortar and pestle and then homogenously mixed with boron nitride to achieve 10 mg of iron in each 1 cm round PTFE sample holder. Sample holders were sealed with Kapton tape, and then impulse-sealed in polyethylene pouches to inhibit oxidation during measurement. Spectra were collected at room temperature (295 K) and at both 13 K and 5 K using a liquid helium cryostat. Samples were measured in transmission with a 10 to 50 mCi ^{57}Co-Rh gamma source on a 1024 channel detector. Measurement time was up to 18 h for each temperature, and all measurements were taken between -11 and +11 mm s^{-1}. Fitting of each spectrum was accomplished using the Voigt based fitting module of the Recoil software package (Lagarec and Rancourt, 1997).

2.5.3. EXAFS Spectroscopy

Samples of the initial synthetic smectites from one replicate in each of the 21% O_2 and hydrogen peroxide oxidation studies were prepared for EXAFS spectroscopy measurements by

sealing the solids in polyimide washers (0.14 mm thick, 4 mm inner diameter, 9.5 mm outer diameter) using Kapton tape. Aluminized Kapton film was then affixed to each sample holder using epoxy as a secondary barrier to prevent exposure to O_2 in air. EXAFS spectra were then measured in transmission at Advanced Photon Source beamline 12-BM-B. The incident beam energy was scanned using a fixed-offset Si (111) double-crystal monochromator. The monochromator was detuned 20% to decrease the harmonic content. A pair of flat and toroidal mirrors defined the beam shape to approximately 1 mm diameter and further decreased the harmonic content. A metallic iron foil was used for energy calibration, with the first maxima in the first derivative set to 7112 eV. Three scans were collected for each sample and averaged in the Athena (Ravel and Newville, 2005) interface to IFEFFIT (Newville, 2001), followed by extraction of the EXAFS spectrum for analysis.

A structural model was refined to each k^3-weighted EXAFS spectrum using Sixpack (Webb, 2005). Backscattering phase and amplitude functions for neighboring atoms were calculated in FEFF 7.02 using the structure of siderophyllite (Redhammer and Roth, 2002). The calculation was performed on a modified structure that included Al, Fe, and Mg as neighboring octahedral cations to provide the necessary fitting components. The amplitude reduction factor, S_0^2, was set to 0.9 for fitting. Data were fitted in R-space between 0.8 and 4.0 Å with a Fourier transform range of 3 to 13 $Å^{-1}$ (Hanning window, dk = 1 $Å^{-1}$). A local coordination model was created consisting of two oxygen neighbors to represent Fe-O interatomic distances expected for Fe(II) and Fe(III). Each oxygen shell was given a coordination number corresponding to octahedral coordination scaled by the fractional abundance of Fe(II) or Fe(III) measured by colorimetry. The neighboring tetrahedral sheet cations were modeled as four Si neighbors. The minor tetrahedral Al component was not explicitly included because it displays similar

backscattering behavior as Si and would have a negligible impact on the fitting results. The adjacent octahedral sheet cations were modeled as Fe, Al, and Mg neighbors having a distribution based on the clay composition and site occupancy, assuming a random distribution. To decrease correlations, the interatomic distance to each was linked to have a single value. Two σ^2 values were fitted, one for the Fe shell and one for the Al and Mg shells because the former likely consists of a mixture of Fe(II) and Fe(III) and is thus expected to have greater apparent positional disorder. Expected differences in Fe-Fe interatomic distance resulting from the distinct ionic radii (Shannon, 1976) of Fe(II) and Fe(III) (0.135 Å) are smaller than the spatial resolution of the data (0.157 Å) and thus cannot be modeled separately.

3. RESULTS

3.1. Characterization of Initial Synthetic Smectites

The compositions of the two synthetic smectites (**Table 2**) are consistent with trioctahedral saponites enriched in iron (April and Keller, 1992; Badaut et al., 1985; Kohyama et al., 1973; Parthasarathy et al., 2003). Layer charge determined from the structural formulas resided solely in the tetrahedral sheet from aluminum substitution for silicon. Despite hosting some aluminum and the small portion of iron that oxidized during synthesis, the trioctahedral sheets have only slight net positive charges because trivalent ion substitutions are largely offset by small vacancy contents. Both smectites have similar octahedral sheet occupancy close to the ideal trioctahedral case. Consistent with previous syntheses of similar phases (Chemtob et al., 2015; Fox et al., 2021), the compositions of the resulting smectites were depleted in magnesium relative to the ratios of components in the initial precipitating solutions. The initial Fe:Mg:Al ratios for the precipitating fluids (**Table 1**) were 40:40:20 and 60:20:20 for the resulting 53:24:23

and 70:08:23 smectites, respectively. In both cases iron and aluminum appear as a higher proportion of the resulting composition relative to magnesium than in the precipitating fluid. XRD patterns for both smectites indicate the presence of no other detectable crystalline mineral phases (**Fig. 1**). Asymmetry seen in some features is typical for turbostratically-stacked phyllosilicates (Brindley and Brown, 1982; Moore and Reynolds, 1997). Positions of the (06,33) *hk* band (**Fig. 1**), corresponding to d-spacings of 1.537 Å for the moderate-iron smectite and 1.546 Å for the high-iron smectite, are consistent with trioctahedral smectites (Moore and Reynolds, 1997), including smectites of similar composition (Chemtob et al., 2015; Fox et al., 2021). The (001) peak positions, corresponding to d-spacings of 16.2 and 16.4 Å for the moderate- and high-iron smectites, respectively, indicate predominantly two layers of water in the Ca-saturated interlayer (Brindley and Brown, 1982; Watanabe and Sato, 1988). The Fe K-edge EXAFS spectra of the initial synthetic smectites (**Fig. S1**) are consistent with the measured compositions and a random distribution of octahedral cations through the clay structures (**Supplementary Material**).

Room temperature Mössbauer spectra for the two smectite compositions (**Fig. 2**) were well fit by a single doublet each for Fe(II) and Fe(III) (**Table 3**). The proportion of Fe(III) to Fe(II) in the synthesized clays determined by Mössbauer spectroscopy were in agreement with colorimetric measurements (**Table 4**). Mössbauer spectra of unoxidized samples at low temperature show a pattern consistent with the nascent emergence of ferrous octets with a magnetic ordering temperature that increases with increasing Fe(II) content (Ballet et al., 1985; Rancourt et al., 1994; Ribeiro et al., 2009; Rothwell, 2019). Spectra of both compositions begin to magnetically-ordered at lower temperatures, with the onset of ordering observed at 13 K for the high-iron smectite and at 5 K for the moderate-iron smectite (**Fig. 2**). These low-temperature

spectra are similar to those of fully-reduced nontronites or other layer silicates with substantial ferrous substitution (Cardile et al., 1986; Rancourt et al., 1994; Stucki, 2011). The partially-ordered ferrous octet at low temperature can be modeled using a Full Static Hamiltonian method, but there is still debate over the interpretation of the parameters (Rothwell, 2019). For our purposes here, which relate mostly to oxidation extent, we only qualitatively interpret these low temperature spectra and focus quantitative interpretation on the 295 K spectra.

3.2. Rates and Extents of Oxidation of Fe(II) in Smectites

3.2.1. Oxidant-free controls

Negligible oxidation of ferrous iron in the smectites occurred during control studies conducted in the absence of oxidants (**Fig. 3**). Measured Fe(II) / Fe(Total) ratios were slightly lower than those obtained during initial characterization, which we attribute to prolonged exposure to traces of oxygen in the anaerobic chamber used for these studies. An increase in pH of ~0.4 units occurred over the course of the experiments (**Table 4**). This is attributed to slight CO_2 degassing after decapping the reactors and measuring the pH in the low-CO_2 atmosphere of the anaerobic chamber, although minor smectite dissolution or surface acid-base chemistry cannot be ruled out as a contributing factor.

3.2.2. Oxidation by Dissolved Oxygen

Dissolved oxygen incompletely oxidizes both smectite compositions, irrespective of oxygen concentration (**Fig. 3**). Oxidation initially proceeded rapidly for both compositions but then slowed despite ferrous iron remaining in the smectite structures. The initial rate and total extent of oxidation were greater for the high-iron composition clay compared to the moderate-

447 iron composition (**Table 5**). Atmospheric O_2 levels produced more rapid oxidation, and
448 oxidation proceeded to a greater extent compared to 2% O_2(g) in the microoxic studies,
449 regardless of smectite composition.
450 Dissolved oxygen levels took several hours to reach equilibrium in both the air-
451 equilibrated and microoxic studies (**Fig. S2**). Pre-equilibration of the solution with O_2 was not
452 possible because the smectites needed to first be suspended and hydrated under anoxic
453 conditions prior to initiating the experiments. Initial gas-water equilibration with O_2 was more
454 rapid in studies using atmospheric oxygen than in the microoxic experiments. This is likely due
455 to high initial rates of consumption by the oxidation of ferrous iron while gas composition and
456 flow rates remained constant. Dissolved oxygen levels after this point remained stable and
457 primarily varied with temperature, which affects oxygen solubility. In each experiment, pH
458 increased by 0.4 to 0.7 units over the course of the experiment (**Table 4**), again likely from CO_2
459 degassing during pH measurement in the anaerobic chamber. The effect was smaller in the
460 microoxic studies, potentially because of increased buffering capacity from the greater CO_2
461 partial pressure in these experiments.
462
463 ***3.2.3. Oxidation by Nitrite***
464 In contrast to reaction with dissolved oxygen, suspensions of both smectites in media
465 containing 5 mmol L^{-1} sodium nitrite showed minimal oxidation over the experimental period of
466 650 hours for the moderate iron smectite and 1302 hours for the high iron smectite (**Table 4**, **Fig.**
467 **4**). The Fe(III)/Fe(Total) of nitrite-exposed samples were generally indistinguishable from
468 oxidant free controls except at long time intervals with the high-iron smectite, with the
469 Fe(II)/Fe(Total) ratio dropping below 0.8 at 580 hours and proceeding to 0.73±0.04 at 1302

hours. For the moderate-iron smectite, no variation in nitrite concentration was observed over the duration of the experiment (**Fig. S3**). An analytical problem prevented quantification of dissolved nitrite for the high-iron concentration experiment. However, the observed iron oxidation requires reduction of only 1.7% of the nitrite in the experiment, smaller than the typical 4.6% standard deviation of nitrite concentrations in the triplicate reactors for the moderate-iron experiment. This amount of nitrite reduction would not have been observable.

3.2.4. Oxidation by Hydrogen Peroxide

Oxidation by hydrogen peroxide resulted in an immediate change in the color of the smectite from blue-green to brown. This reaction was accompanied by the release of a substantial amount of gas, presumably O_2 although this was not measured. The extent of oxidation in the smectite measured colorimetrically and by Mössbauer spectroscopy were in close agreement (**Table 4**), with both showing 3 to 6 % residual Fe(II) remained after oxidation by hydrogen peroxide.

3.3. Analysis of Oxidation Kinetics

A two site second-order kinetic model (**Equations 1, 2**) was fit to each dataset for oxidation by O_2 (**Table 5**). Fast and slow oxidation components as well as a recalcitrant Fe(II) fraction were independently fitted for the high-iron smectite results. For the high-iron smectite, the rapid component had a rate constant ~5 times greater at 21% O_2 compared to 2% (**Table 5**). While this may suggest kinetic behavior that is not first-order with respect to oxygen partial pressure, dissolved oxygen concentrations took 1 to 4 h to equilibrate with the gas stream; this period of unbuffered oxygen partial pressure was not accounted for in the model. Data at short

493 reaction times (<3 h) was not obtained for the moderate-iron smectite at both O_2 concentrations
494 and this prevented accurate fitting of the rate constant for the fast oxidation component (k_1). This
495 parameter was fixed to the value obtained from the high-iron smectite experiments using the
496 same O_2 concentration (**Table 5**). This precludes comparison of the rate of the rapid component
497 (k_1) between two clays.

498 The fraction of oxidized Fe(II) modeled by the fast component (a_1) was greatest for the
499 high-iron smectite oxidized by air, with this contribution decreasing under lower oxygen partial
500 pressure and for the moderate-iron smectite. The moderate-iron smectite reacted with 2% O_2
501 contained a substantially lower initial Fe(II) concentration than the same smectite immediately
502 after synthesis or in the other experiments (**Table 4**). Kinetic modeling of the oxidation of the
503 moderate-iron smectite by 2% O_2 required only a small contribution of the fast oxidation
504 component (i.e., a small a_1 value). We hypothesize that inadvertent partial oxidation occurred
505 during the setup for this specific experiment, and that a portion of the fast-reacting Fe(II) pool
506 was consumed before our measurements were initiated.

507 For each smectite, the modeled slow oxidation component of the kinetic behavior
508 accounted for a similar fraction of Fe(II) oxidation under both oxygen levels (**Table 5**). Kinetic
509 modeling produced a smaller recalcitrant Fe(II) fraction for the high-iron smectite compared to
510 the moderate-iron smectite (**Table 5**), consistent with observed differences total Fe(II) oxidation
511 (**Fig. 3**). For both clays, the modeled recalcitrant fraction was greater for experiments with 2%
512 O_2 than with 21% O_2 (**Table 5**). This indicates that slower overall reaction rates, as produced by
513 lower Fe(II) contents or O_2 concentrations, generate greater fractions of recalcitrant Fe(II).

514 The modeled extent of oxidation in the control experiments, as well as the nitrite-exposed
515 experiment with the moderate-iron smectite, was equal to or within error of zero. We evaluated

this behavior using a single first-order kinetic term with a recalcitrant portion (see **Supplementary Material**). For the oxidant-free control experiments, the model-obtained rate constants were effectively zero after considering parameter uncertainty (**Table S3**), confirming that no detectable oxidation occurred over the duration of these control experiments. Reaction of the moderate-iron smectite with nitrite yielded a rate constant that was the same order of magnitude as, but smaller than, its uncertainty, indicating that no statistically-significant oxidation occur on the experimental timescale. Reaction of the high-iron smectite with nitrite was the only system to produce a rate constant that was not within error of zero (**Table S3**, **Fig. S4**). However, accurately quantifying the rate of oxidation of this clay by nitrite would require experiments longer than the 54-d duration explored in this study because of the slow reaction rate.

3.4. Characterization of Oxidation Products

3.4.1. Powder X-ray Diffraction

No features from crystalline secondary minerals were observed in the XRD patterns of the oxidized smectites but diffraction features associated with layer stacking and lattice size shifted systematically (**Fig. 5, 6**). The (001) peak positions (**Fig. 5**) of the smectites show a general shift to higher angle with increasing extent of oxidation (**Table 6**), resulting in a decreased in d-spacing (**Fig. 7**). The (001) d-spacing for the initial synthetic smectites is systematically larger than for the reacted smectites, deviating from the trend with increasing iron oxidation extent. This reflects differences in drying between the initial smectites and the reacted smectites. While both were dried in a vacuum desiccator, the initial smectite samples had substantially larger masses (~5 g) than the reacted samples (<200 mg) and thus reached different

539 extents of dehydration during similar desiccation times. In addition, suspension in the media
540 solution during the oxidation experiments alters the interlayer cation composition (this was not
541 measured) compared to the initially Ca-saturated smectites, which also impacts the (001) d-
542 spacing. All of the smectites used in oxidation experiments experienced the same fluid
543 composition and drying procedures and the observed trend among these reacted samples is thus
544 robust. The (06,33) *hk* bands (**Fig. 6**) also shift to higher angle after oxidant exposure (**Table 6**),
545 corresponding with a shift towards smaller *b* unit cell parameters. This results from Fe(II) in the
546 octahedral sheet oxidizing to Fe(III), which has a smaller ionic radius (Shannon, 1976). The
547 high-iron smectite displays a more linear relationship between (06,33) d-spacing and extent of
548 oxidation than the moderate-iron smectite (**Fig. 7**). All changes to the XRD patterns of the
549 smectites were greatest after reaction with hydrogen peroxide and smallest after reaction with
550 nitrite, showing that oxidation extent (**Table 4**) is the primary cause of structure change.
551
552 ***3.4.2. Mössbauer Spectroscopy***
553 Spectra collected at 295 K (**Fig. 8, 9**) show only paramagnetic ordering and a transition
554 from primarily an Fe(II) doublet to an Fe(III) doublet with increasing extent of oxidation. These
555 spectra were thus modeled with one Fe(II) and one Fe(III) site using the Voigt-based fitting
556 module in Recoil (**Table 3**). The resulting Fe(II) and Fe(III) contents were consistent with the
557 extents of oxidation determined by the colorimetric measurements for the oxygen-exposed and
558 control samples (**Table 4**). For both smectites, greater oxidation extent correlated with a smaller
559 quadrupole splitting of the Fe(II) site (**Fig. 10**). The Mössbauer-derived Fe(III) content for one
560 sample (the nitrite-exposed, high-iron sample) was substantially larger than the value determined
561 from colorimetry (**Table 4**). We hypothesize that inadvertent oxidation of this sample occurred

562 during prolonged storage between the experiments, during which colorimetric analysis occurred,
563 and the Mössbauer measurements.

564 The 13 K and 5 K Mössbauer spectra of smectites reacted with oxidants (**Fig. 8, 9**) are
565 consistent with layered silicate clays with high iron substitution and spectral features that vary in
566 response to the Fe(III) and Fe(II) content (Ballet et al., 1985; Rancourt et al., 1994; Ribeiro et al.,
567 2009; Rothwell, 2019). This includes the emergence of magnetic coupling and ordering (or
568 partial ordering) at low temperatures (generally <13 K) arising principally from magnetic
569 interactions between Fe atoms in next-nearest neighbor positions, for example Fe-O-Fe. Such
570 superexchange (Ballet et al., 1985) may result from the high Fe content. The partially ordered
571 ferrous octet observed in the initial smectites at 5K persists after exposure to nitrite but with the
572 emergence of a partially-collapsed ferric iron sextet for the high-iron smectite (**Fig. 8, 9**). For the
573 oxygen-exposed and hydrogen peroxide samples, the spectra contain a larger Fe(III) component
574 and the ferrous-magnetic ordering is lost (**Fig. 8, 9**). In the oxygen-exposed moderate-iron
575 smectite, this ferric component persists as a doublet down to 5K, with some evidence of a
576 collapsed feature in the less reduced (2% and 21% O_2) samples that may indicate Fe clustering
577 (Ballet et al., 1985; Rothwell, 2019). For the high-iron smectite samples, the Fe(II) and Fe(III)
578 doublets are overlain by a weakly-formed and partially collapsed Fe(III) sextet (**Fig. 9**). The
579 samples exposed to hydrogen peroxide displayed the greatest amount of Fe(III) for both the high-
580 and moderate-iron compositions, comprising >94% of the iron in each sample (**Table 4**) and
581 show a strong doublet component in the 5 K spectra and a similar partially collapsed Fe(III)
582 sextet at 5 K for the high-iron sample.

583 Many layered silicates have low to moderate Fe substitution levels and do not exhibit any
584 hyperfine field splitting or magnetic ordering in their Mössbauer spectra at 5 K. The spectra of

585 these typical clay minerals contain only ferric or ferrous doublets. Any sextets in Mössbauer
586 spectra of such low-iron clay samples (even partially-ordered sextets) suggest the presence of
587 secondary Fe-oxide phases. Exceptions to this assumption occur at both at the extreme low-end
588 of Fe substitution, where some non-parametric relaxation can produce a broad sextet (Murad and
589 Cashion, 2004), or at high levels of substitution where clusters of Fe atoms can interact through
590 superexchange and produce hyperfine field splitting and partial or full magnetic ordering (Murad
591 and Cashion, 2004; Rancourt et al., 1994). The latter case applies to the smectites in the present
592 study.

593 Distinguishing Fe atoms in iron-rich (or extremely iron-poor) layered silicates from
594 secondary iron (oxyhydr)oxides, both of which can exhibit hyperfine ordering at 5 K, using
595 Mössbauer spectroscopy requires collection of spectra at temperatures intermediate between
596 ambient and 5 K (Chen et al., 2017). For Fe(III) atoms in layered silicates, any hyperfine
597 splitting or magnetic ordering present at 5 K usually disappears at 12 K, whereas short-range-
598 ordered iron oxyhydroxides (e.g., ferrihydrite) typically retain magnetic ordering until
599 temperatures exceed 35 to 77 K (Sun et al., 2018; Whitaker et al., 2021). Even the most highly
600 substituted or nanosized short-range-ordered iron oxyhydroxides will nearly always exhibit at
601 least partial ordering by 12 K (Chen et al., 2018; Noor and Thompson, 2022). Thus, by collecting
602 spectra at both 4 to 5 K and 12 to 13 K, Fe(III) in silicates and Fe(III) in secondary oxides can
603 distinguished.

604 For the samples studied here, oxidation of the moderate-iron smectites, even with H_2O_2,
605 do not produce hyperfine field splitting of Fe(III) atoms at either 13 K or 5 K (**Fig. 8**). We can
606 reasonably conclude that no secondary iron oxides or short-range-ordered iron(III)
607 oxyhydroxides were produced and the Fe(III) exists in generally similar (or uniformly

608 distributed) sites. For the oxidized high-iron smectites, the hyperfine field for one or two Fe sites
609 are split and near their ordering temperature at 5 K (**Fig. 9**). Progressively more oxidized
610 samples (2% O_2, 21% O_2, and H_2O_2 treatments) have similar features so we can evaluate the
611 H_2O_2 sample where near-complete oxidation has occurred. The 5 K Mössbauer spectrum of the
612 H_2O_2-oxidized sample contains an Fe(III) sextet with a low field strength (hyperfine field:
613 42.3±0.2 T, chemical shift: 0.47±0.02 mm s^{-1}, quadrupole splitting: -0.04±0.02 mm s^{-1}), a
614 collapsed Fe(III) sextet, and an Fe(III) doublet (chemical shift: 0.47±0.2 mm s^{-1}, quadrupole
615 splitting: 1.00±0.02 mm s^{-1}). This could reflect Fe(III) occupying three different sites with the
616 doublet representing isolated Fe(III) atoms (likely in the octahedral sheet), and the full and
617 collapsed sextets representing Fe with two (Fe-O-^{57}Fe-O-Fe) or one (Fe-O-^{57}Fe) next nearest
618 neighbors. The collapsed sextet could also reflect adsorbed Fe(III), perhaps in interlayer sites
619 after partial dissolution of the clay and ion-exchange into the interlayer before or after oxidation.
620 The lack of any hyperfine splitting at 13 K strongly argues against a distinct short-range-ordered
621 Fe oxyhydroxide. This spectral interpretation is consistent with a prior study of reduced, re-
622 oxidized dioctahedral smectites (Ribeiro et al., 2009), which displayed a better developed Fe(III)
623 sextet at 4 K than observed in the present study without formation of secondary Fe(III)
624 oxyhydroxides.
625
626 ***3.4.3. EXAFS Spectroscopy***
627 The Fe K-edge EXAFS spectra of the smectites after oxidation by 21% O_2 or H_2O_2 show
628 consistent spectral changes compared to the initial smectites (**Fig. 11**). The Fourier transform
629 feature near 1.7 Å shifts inward by ~0.15 Å, consistent with the expected contraction from
630 oxidation of Fe(II) to Fe(III). The second shell feature near 2.8 Å decreases in amplitude, which

631 can be produced by a decrease in the number of octahedral or tetrahedral neighbors, increased
632 positional disorder among the iron sites, or increased destructive interference between the
633 spectral contributions from the octahedral and tetrahedral cation neighbors. A structural model
634 (described in Section 2.6) that retains all iron in the octahedral sheet well reproduces the
635 observed changes in the spectra (**Fig. 11**). This explicitly models the first shell feature as a
636 mixture of Fe(II)-O and Fe(III)-O interatomic distances proportioned by the iron oxidation state
637 quantification via colorimetry (**Table S2**). The octahedral cation neighbors maintain the relative
638 abundances of Fe, Al, and Mg predicted from the clay compositions for a random distribution of
639 neighbors. The structural model identifies increased disorder of both Fe-Fe and Fe-Si interatomic
640 distances following oxidation (**Table S2**). Distinct interatomic distances likely result for Fe(III)
641 in cis and trans sites within the octahedral sheet, creating substantial disorder in the EXAFS
642 spectra, which represents an average structure over all sites. A slight decrease in the differences
643 in interatomic distances between Fe and octahedral versus tetrahedral neighbors (**Table S2**)
644 creates increased destructive interference that is partially responsible for the decreased intensity
645 of the second shell feature in the Fourier transform spectra (**Fig. 11**).
646
647 **4. DISCUSSION**
648 **4.1. Products of Trioctahedral Smectite Oxidation**
649 ***4.1.1. Bulk and Local Structural Changes***
650 The XRD patterns of the oxidized smectites from our experiments reveal minor changes
651 in the smectite structure (**Fig. 5**). Among the reacted smectite samples, a decrease in (001) d-
652 spacing is observed for increasing extents of oxidation (**Fig. 7**). The transition of iron from
653 divalent to trivalent form would increase the net positive charge on the octahedral sheet, shifting

654 the net layer charge to a less negative/more positive value. Similar decreases in the negative total
655 layer charge of smectites have previously been associated with a decrease in expandability
656 (Komadel et al., 2005). While oxidation did not result in interlayer collapse, with the samples
657 taking on a talc- or illite-like structure, the systematic decrease in d-spacing is likely a direct
658 effect of the change in layer charge following oxidation. All reacted smectites were exposed to
659 identical aqueous solution compositions and experienced identical drying conditions prior to
660 XRD analysis, ruling out experimental artifacts as a cause of the observed variations.
661 Oxidation also impacted the in-plane structure of the smectites. The (06,33) *hk* bands
662 (**Fig. 6**) of the oxidized smectites shift towards smaller d-spacings with increased oxidation
663 (**Table 6**). There is no evidence of iron ejection from the structure associated with oxidation. No
664 new crystalline phases, such as goethite, appear in the XRD patterns (**Fig. 5**). Similarly, the 13 K
665 Mössbauer spectra of the oxidized samples (**Fig. 8, 9**) show no evidence of sextets, which would
666 be expected for all but the most disordered short-range-ordered iron phases and even then partial
667 ordering would likely be evident (Noor and Thompson, 2022). Further, the EXAFS spectra (**Fig.**
668 **11**) are consistent with full retention of iron in the octahedral sheet. These exclude substantial
669 migration of iron into the clay interlayer, a possible explanation of a collapsed feature
670 component in some 5 K Mössbauer spectra. Contributions from a collapsed features are weaker
671 in the Mössbauer spectra of the moderate-iron smectite, including being absent after oxidation by
672 H_2O_2, but this should generate stronger second shell features in the EXAFS spectra for this clay
673 than for the high-iron smectite, the opposite of what is observed (**Fig. 11**). Together, these
674 observations imply that a trioctahedral structure was retained after oxidation. Note that these
675 methods cannot rule out a small fraction of iron (a few percent at most) forming a discrete

676 secondary phase, but this would make a negligible contribution to the overall fate of iron as 57 to
677 95% oxidizes upon exposure to O_2 or H_2O_2 (**Table 4**).
678 Retention of nearly all iron following oxidation poses a challenge for maintaining charge
679 balance in the structure. For example, recalculation of layer charge using the initial structural
680 formulae (**Table 2**) but with the observed Fe(II)/Fe(Total) ratios after oxidation by 21% O_2
681 would increase the total charge from -0.34 to +1.24 for the moderate-iron smectite and from -
682 0.40 to +1.44 for the high-iron smectite. While an octahedral sheet in a smectite may hold a
683 positive charge if offset by a negative charge on the tetrahedral sheet, a positive total layer
684 charge is not possible for a 2:1 clay structure. The available data cannot unambiguously identify
685 a charge-compensation mechanism, but near-complete iron retention and preservation of 6-
686 coordinated sites suggest that substantial deprotonation of octahedral sheet hydroxyl groups
687 accompanies oxidation.
688
689 ***4.1.2. Redox Distribution, Magnetic Ordering, and Secondary Phases***
690 Direct attribution of doublets in Mössbauer spectra to specific octahedral iron sites has
691 been shown to be difficult, often leading to inaccurate ratios of sites (Baron et al., 2017; Dyar et
692 al., 2008; Heller-Kallai and Rozenson, 1981; Rancourt, 1994a, b). The majority of the iron
693 incorporated into the clay structure was initially present as Fe(II), with only 6 to 8 mol. % as
694 Fe(III). The low Fe(III) contents of the synthetic clays makes it unlikely that tetrahedral iron is
695 present in the smectite structure, consistent with the single ferric doublet modeled for each initial
696 sample. Ferrous CS values (**Table 3**) were similar to those previously reported for synthetic
697 trioctahedral ferrous smectites (Chemtob et al., 2015) and quadrupole splitting values were
698 intermediate of the two sites used in the modeling in that work. Ferric parameters (**Table 3**) are

699 similarly within the range of ferric values previously reported for oxidized trioctahedral
700 smectites (Chemtob et al., 2017).
701 While prior work has examined the cryogenic Mössbauer spectra of Fe(II) in
702 trioctahedral mica, chlorite, and serpentine minerals (Ballet et al., 1985; Rancourt et al., 1994),
703 this study is the first to report low-temperature spectra from Fe(II)-bearing trioctahedral
704 smectites. Previous studies have obtained room temperature Mössbauer spectra of natural
705 (Badaut et al., 1985; Kohyama et al., 1973) and synthetic (Chemtob et al., 2015) ferrous
706 smectites. All show similar parameters to the 295 K measurements reported in the presented
707 work, including for the minor ferric component. Reduced dioctahedral smectites provide an
708 additional comparison, with 4 K Mössbauer spectra of a fully reduced sample of the Garfield
709 nontronite (Ribeiro et al., 2009) displaying magnetic ordering of ferrous iron similar to the
710 unoxidized trioctahedral ferrous smectites measured at 5 K in our study. This similarity is
711 consistent with reduction of iron-rich dioctahedral smectites producing trioctahedral domains in
712 the mineral structure (Drits and Manceau, 2000; Fialips et al., 2002b; Manceau et al., 2000a;
713 Manceau et al., 2000b).
714 The observed relationship between oxidation extent and quadrupole splitting of the Fe(II)
715 site (**Fig. 10**) is consistent with the behavior displayed by a natural ferrous smectite as it oxidized
716 (Kohyama et al., 1973). This was suggested to indicate that the oxidized smectite had less
717 distortion surrounding the iron sites than unoxidized smectite. This interpretation matches the
718 effect on quadrupole splitting observed in the octahedrally-coordinated Fe(II) in micas when
719 compressed to 200 kbar (Huggins, 1976). It also agrees with simulations showing that greater
720 distortion of the octahedral sheet of phyllosilicates results in a greater quadrupole splitting for
721 Fe(II) in the structure (Evans et al., 2005). The observed trend in quadrupole splitting (**Fig. 10**)

thus suggests that the remaining Fe(II) in more oxidized smectites exists within a less distorted local environment. This could result from the structural shifts following oxidation, i.e., in-plane lattice contraction, but may also indicate that two Fe(II) sites were present in the structures and the more distorted site preferentially oxidizes. The quadrupole splitting of Fe(III) within the samples increases slightly with the extent of iron oxidation (**Fig. 10**), suggesting a more disordered environment, consistent with the EXAFS results. Similar observations were made in prior work on natural oxidized trioctahedral smectites (Kohyama et al., 1973). Study of native Fe(III) in trioctahedral phyllosilicates is limited but generally finds less variation in the quadrupole splitting of Fe(III) than in dioctahedral phases (Heller-Kallai and Rozenson, 1981).

4.1.3. Evolving Distribution of Iron Species in the Smectite Structure

Exposure to nitrite, O_2, and H_2O_2 produced different extents of iron oxidation, creating an array of different local iron coordination environments (**Fig. 12**). The random distribution of iron throughout the clay structures, as indicated by EXAFS spectroscopy, suggests that the initial Fe(II) present occurred in an array of local coordination environments resulting from the complex composition of the smectites. While this was only slightly perturbed by exposure to nitrite, oxidation by O_2 converted a substantial fraction of Fe(II) to Fe(III). A complex mixture of iron species distributed throughout the structure resulted from oxidation, including varying amounts of octahedral Fe(II)-Fe(II), Fe(II)-Fe(III), and Fe(III)-Fe(III) neighbors. The recalcitrant Fe(II) fraction that remained preferentially resides in less distorted sites, as indicated by Mössbauer spectroscopy, but the nature of such sites cannot be ascertained because of the abundant Fe(III) that co-occurs and produces the dominant signal source in all spectroscopic methods employed. The evolution of the local coordination environment around iron species in

745 the clay structure involves both contraction of neighboring iron sites as they oxidize and an
746 increase in positive charge, possibly accompanied by hydroxyl deprotonation.
747
748 **4.2. Controls on the Extent and Rate of Oxidation by Dissolved Oxygen**
749 Among the two compositions used in our study, the high-iron smectite exhibited a greater
750 portion of the most reactive Fe(II) species and less nonreactive Fe(II) relative to the moderate-
751 iron smectite. A prior study of trioctahedral smectite oxidation after 7 days of exposure to O_2
752 similarly found that greater Fe(II) content resulted in a greater fractional amount of oxidation
753 (Chemtob et al., 2017). This behavior aligns with observations of reduced dioctahedral smectites,
754 where neighboring cations impact the oxidation rates of Fe(II) and trioctahedral Fe(II)-Fe(II)-
755 Fe(II) clusters show the greatest reactivity (Neumann et al., 2011). The greater iron content in the
756 octahedral sheet of the high-iron smectite should result in a greater number of trioctahedral
757 Fe(II)-Fe(II)-Fe(II) clusters. This relationship between iron content and trioctahedral Fe(II)
758 clusters assumes that iron is randomly distributed throughout the octahedral sheet, which is
759 supported by the EXAFS spectroscopy results. This contrasts with Fe(III)-bearing dioctahedral
760 smectites that display either preferential (i.e., non-random) iron clustering or avoidance
761 (Vantelon et al., 2003; Vantelon et al., 2001).
762 Changes in iron redox potential across different octahedral sites with different
763 neighboring cations within the smectite may also contribute to the observed kinetic behavior and
764 recalcitrant Fe(II) pool. Iron in dioctahedral smectites displays a non-Nernstian redox potential
765 which varies alongside a variety of structural parameters (Gorski et al., 2012; Gorski et al.,
766 2013). The underlying cause of this behavior is not fully known but may be due to either non-
767 unity activity for different iron species or changes in the variety of local coordination

768 environments that iron exists in within the smectite structure. This non-Nernstian redox behavior
769 has been shown to effect the kinetics of U(VI) reduction by Fe(III) in a nontronite (Luan et al.,
770 2014), resulting in a fast-reacting iron fraction, a slower fraction, and a non-reactive fraction.
771 The exact potentials are dependent upon the specific smectite but studies of reduced dioctahedral
772 smectites have not measured potentials positive enough to inhibit oxidation by oxygen (Gorski et
773 al., 2012; Gorski et al., 2013). In addition, reduced dioctahedral smectites are observed to
774 completely re-oxidize in air (Komadel et al., 1990; Komadel et al., 1995; Ribeiro et al., 2009;
775 Stucki, 2011). The range of redox potentials for iron in trioctahedral ferrous smectites remains
776 unexamined, but the incomplete extent of oxidation observed in this study suggests that these
777 sites also have non-Nernstian redox potentials, and that these potentials may be shifted towards
778 higher voltages than observed for dioctahedral smectites. We hypothesize that the occurrence of
779 recalcitrant Fe(II) is primarily a thermodynamic phenomenon. Mössbauer spectroscopy indicate
780 that this species occurs in a symmetric octahedral site, although further characterization is not
781 possible with available methods. The presence of multiple Fe(III) neighbors represents a
782 potential stabilization mechanism because this would create a local environment with excess
783 positive charge, making further oxidation less favorable.
784 Non-Nernstian redox potentials in smectites, however, do not explain the variation in
785 extent of oxidation observed for each smectite under different oxygen concentrations. The
786 differences in the concentrations investigated in this study only have minor effects on the redox
787 potential (~0.015 V variation for the O_2/H_2O couple). Considering the redox potential behavior
788 displayed by reduced dioctahedral smectites (Gorski et al., 2013), this small variation in oxidant
789 redox potential would result in <2% difference in the fraction of Fe(II) oxidized, whereas the
790 experiments reveal a 7% difference for the high-iron smectite and a 19% difference for the

791 moderate-iron smectite. The inverse correlation between oxidation rates and recalcitrant Fe(II)
792 fractions indicates that creating such a stable ferrous iron pool involves a mechanism occurring
793 on timescales similar to oxidation reactions. Possible Fe(II) stabilization mechanisms include
794 deprotonation of hydroxyl sites, migration of interlayer cations to offset charge creation during
795 oxidation, or interconversion of Fe(II) and Fe(III) sites through electron transfer (Neumann et al.,
796 2008). In such a scenario, the amount of recalcitrant Fe(II) reflects competition between two
797 reaction pathways: Fe(II) oxidation and Fe(II) site stabilization. The size of the recalcitrant iron
798 pool may thus record the rate of oxidation, providing an indirect proxy for oxygen concentration.
799 This could be further evaluated through oxidation rate measurements at lower oxygen partial
800 pressures coupled to computational studies to identify Fe(II) species in the octahedral sheet most
801 resistant to oxidation.
802
803 **4.3. Limited Reactivity of Structural Fe(II) with Nitrite**
804 Over the time period examined in this study (650 h), nitrite did not detectably oxidize the
805 iron present in the moderate-iron smectite. A small degree of oxidation was observed in the high-
806 iron smectite: 17±4% after 1302 hours (**Fig. 4**). Note that this experiment was conducted for a
807 substantially longer duration than studies of the same smectite in the air-equilibrated and
808 microoxic studies (432 to 650 hours) in order to observe this partial oxidation. When comparing
809 over the same reaction times, 10% of the Fe(II) in high-iron smectite exposed to nitrite oxidized
810 compared to 78% and 60% in the air-equilibrated and micro-oxic samples, respectively. This
811 demonstrates that although nitrite was present at ~18 times the maximum dissolved oxygen
812 concentration used in this study ($pO_2 = 0.21$ corresponds to 0.28 mmol L^{-1} dissolved O_2) it
813 oxidizes Fe(II) in trioctahedral smectites at a far slower rate.

814 Minimal abiotic oxidation of Fe(II) in a reduced nontronite by nitrite was observed under
815 neutral pH conditions during a 17 d (408 h) growth period (Zhao et al., 2013). This is largely
816 consistent with our observations of no detectable oxidation in the moderate-iron smectite and
817 oxidation within error of the oxidant-free control on a similar timescale for the high-iron smectite
818 (**Fig. 4**). A separate study observed substantial abiotic nitrite reduction in the presence of reduced
819 nontronite over ~300 h reaction period (Grabb et al., 2017). Those studies employed a large
820 excess of clay Fe(II) relative to nitrite (32.9 mM Fe(II) versus 0.13 mM nitrite) whereas the
821 present work utilized nitrite in stoichiometric excess (~1 mM Fe(II) versus 5 mM nitrite). This
822 enabled rate determination via nitrite consumption, producing rate constants of 0.003 to 0.005 h^{-1}
823 for reaction with reduced nontronite (Grabb et al., 2017) versus 0.0009±0.0008 h^{-1} was for the
824 high-iron trioctahedral smectite and an unmeasurable rate for the moderate-iron smectite (**Table**
825 **S2**). This demonstrates that natively Fe(II)-bearing trioctahedral smectites react substantially
826 slower with nitrite then reduced, and originally Fe(III)-bearing, dioctahedral smectites.
827
828 **4.4. Implications for Biogeochemical Iron Cycling**
829 The retention of Fe(III) in the mineral structure following oxidation indicates that
830 authigenic, trioctahedral Fe(II) smectites may be capable of repeated oxidation-reduction cycles
831 in the same manner as nontronite and other Fe(III)-bearing smectites (Fialips et al., 2002a;
832 Komadel et al., 1990; Komadel et al., 1995; Manceau et al., 2000a; Manceau et al., 2000b; Zhao
833 et al., 2015). Trioctahedral smectites may thus represent an additional biogeochemical battery
834 (Byrne et al., 2015) widely available on the early Earth. However, unlike dioctahedral smectites,
835 the trioctahedral smectites in this study only partially oxidized upon prolonged exposure to
836 oxygen, suggesting that not all iron in the structure is accessible to redox cycling. Further, the

impacts of re-reduction on trioctahedral smectite stability is currently unknown. Long oxidizing periods may affect redox cycling in these clays because the excess positive charge produced following oxidation may drive eventual conversion to other products. A prior study (Chemtob et al., 2017) exposed similar smectites to dissolved oxygen for 6 d, hydrothermally recrystallized the products at 200°C, and then carried out a second oxidation cycle. Recrystallization increased the susceptibility towards oxidation, which may indicate that post-oxidation structural resetting would alter the extent of redox cycling possible. Hydrothermal treatment did not generate any new phyllosilicates and a smectite structure was preserved, although hematite formed during heating of a partially-oxidize iron-rich smectite (Chemtob et al., 2017). The rate of restructuring of oxidized trioctahedral smectites at non-hydrothermal temperatures is unclear and relatively rapid redox cycling, such as by microbial communities at redox interfaces, may be able to proceed without the clay structure being substantially altered.

The rate of abiotic oxidation of trioctahedral Fe(II) smectite suggests that these phases represent potential electron donors for microorganisms. Recent work (Zhou et al., 2022) has shown that one of the trioctahedral smectites from the present study was able to support the growth of a microaerophilic Fe(II)-oxidizing bacterium. The rate of microbial oxidation was not always faster than abiotic oxidation in the same system. However, the organism expressed outer membrane proteins capable of conducting electron transfer with minerals only when grown on smectites and not with dissolved Fe(II), consistent with microbial utilization of smectite Fe(II). Access to the recalcitrant Fe(II) pool observed in the present work could not be investigated because the organism investigated loses viability beyond 15 d of incubation. The potential for biological utilization of recalcitrant Fe(II) by microaerophilic Fe(II)-oxidizing bacteria could be evaluated using a smectite pre-oxidized by O_2.

Irrespective of the accessibility of the recalcitrant Fe(II) pool, a series of studies now indicate that structural Fe(II) in smectites and other phyllosilicates is accessible to microbial oxidation under microaerophilic conditions (Benzine et al., 2013; Shelobolina et al., 2012a; Zhou et al., 2022). Such microbially-mediated oxidation may be pervasive in altered oceanic crust where ferrous smectites frequently coat cracks and vesicles (Alt and Teagle, 2003; Andrews, 1980; Colwell and D'Hondt, 2013). This large Fe(II) pool may also have served as a crustal redox buffer in ocean basins on the early Earth. In addition, detrital Fe(II)-bearing smectites (Hao et al., 2017) may have provided a regular electron donor source to microoxic oases predicted to have transiently occurred in surface waters prior to the Great Oxidation Event (Canfield, 2005; Riding et al., 2014) even after dissolved Fe(II) was locally consumed.

The exceedingly slow reaction of Fe(II)-bearing trioctahedral smectites with nitrite indicates that these phases are promising potential electron donors for iron-oxidizing, nitrate-reducing bacteria. The intermediate nitrogen species nitrite is highly reactive with dissolved Fe(II), confounding biological coupling of iron oxidation and nitrate reduction (Klueglein and Kappler, 2013; Klueglein et al., 2014). Nitrite also abiotically oxidized iron(II)-bearing reduced, dioctahedral smectites (Grabb et al., 2017), but the present study demonstrates that the abiotic rate of reaction is substantially slower for trioctahedral smectites. Potential abiotic reaction with nitrite makes it unclear whether oxidation of iron in reduced nontronites by nitrate reducers (Benzine et al., 2013; Shelobolina et al., 2012a; Shelobolina et al., 2003) accurately predicts the ability of these organisms to utilize trioctahedral ferrous smectites. A study using the trioctahedral, Fe(II)-bearing mica biotite indicates that such organisms induce a small amount of oxidation during nitrate reduction (Shelobolina et al., 2012b). Substantially greater oxidation

may be possible in trioctahedral smectites because the high crystallinity and larger particle size of biotite should limit reactivity of that mineral.

Redox cycling of trioctahedral smectites will produce distinct effects on isotopic and mineralogical signatures of past biological activity in the rock record. Retention of Fe(III) in the clay structure precludes iron isotope fractionation occurring during oxidation. Smectite iron isotope records should reflect either conditions during clay formation or recrystallization during later diagenesis or metamorphism. Oxidized trioctahedral smectites may, however, leave distinct mineralogical products compared to natively dioctahedral smectites that underwent redox cycling. Iron reduction in dioctahedral smectites increases layer charge and can lead to eventual illitization (Jaisi et al., 2011; Kim et al., 2004; Koo et al., 2014). In contrast, iron oxidation in trioctahedral smectites decreases the layer charge of the smectite. Diagenesis or metamorphism may thus generate iron-rich talc, ferripyrophyllite, chlorite, or stilpnomelane from oxidized trioctahedral smectites.

5. CONCLUSIONS

Fe(II)-bearing trioctahedral smectites display distinct reactivity towards different oxidants (**Fig. 12**). Nitrite induces minimal oxidation of structural Fe(II) while hydrogen peroxide, and thus likely reactive oxygen species, causes near-complete conversion to Fe(III). Abiotic reaction with dissolved oxygen, however, consistently leaves an unreactive Fe(II) pool in the smectite, even after nearly a month of oxidant exposure. This recalcitrance is supporting by kinetic modeling, which cannot describe the time-dependent oxidation behavior without including a portion of Fe(II) that is unreactive. Both the reactivity towards oxidants and incomplete extent of Fe(II) oxidation displayed by trioctahedral smectites are distinct behaviors

905 from reduced dioctahedral smectites, indicating the role of mineral structure in controlling the
906 redox behavior of iron-bearing phases.

907 The Fe(III) generated during oxidation remains in the clay structure, suggesting that
908 trioctahedral smectites are capable of redox cycling. The rates of abiotic oxidation indicate that
909 these minerals represent potential electron donors for microaerophilic iron oxidizing and iron-
910 oxidizing, nitrate-reducing bacteria. It is currently unclear whether the chemically-recalcitrant
911 Fe(II) pool is available for biological utilization. Trioctahedral, Fe(II)-bearing smectites
912 represent important components of the iron biogeochemical cycle during the progressive
913 oxidation of the surface of the Earth and potentially serve as redox buffers in altered oceanic
914 crust. The impact of iron redox changes on layer charge in trioctahedral smectites suggests that
915 diagenesis or metamorphism will leave mineral products in the rock record that are distinct from
916 natively dioctahedral smectites.

917

918 **ACKNOWLEDGEMENTS**

919 This project was supported by the U.S. National Aeronautics and Space Administration
920 (NASA) Exobiology Program through award no. 80NSSC18K129. Additional support was
921 provided by the McDonnell Center for the Space Sciences at Washington University and by the
922 NASA Astrobiology program through award no. 80NSSC19M0069. This research used
923 resources of the Advanced Photon Source, a U.S. Department of Energy (DOE) Office of
924 Science user facility operated for the DOE Office of Science by Argonne National Laboratory
925 under Contract No. DE-AC02-06CH11357. The authors thank Paul Carpenter for assistance with
926 XRD measurements, Elaine Flynn for assistance with ICP-OES measurements and anaerobic
927 chamber maintenance, and Sungsik Lee for managing remote operation of EXAFS data

928 collection at the Advanced Photon Source. Comments from Associate Editor Hailiang Dong and
929 four anonymous reviewers improved this manuscript.

930

931 **DATA AVAILABILITY**

932 Data are available through Mendeley Data at https://doi.org/10.17632/8j3v4s9bs8.2.

933

934 **APPENDIX A. SUPPLEMENTARY MATERIAL**

935 The Supplementary Material document contains full details of the media composition, EXAFS
936 fitting results, time-series data for dissolved oxygen concentrations and temperature during the
937 oxidation experiments investigating O_2, dissolved nitrite concentrations during the experiment
938 with the moderate-iron smectite, and kinetic fitting results for the nitrite and oxidant-free control
939 experiments.

940

941 **REFERENCES**

942 Alt, J.C., 1999. Very low-grade hydrothermal metamorphism of basic igneous rocks, in: Frey,
943 M., Robinson, D. (Eds.), Low-Grade Metamorphism. Blackwell Publishing, Oxford, pp.
944 169-201.
945 Alt, J.C., Honnorez, J., Laverne, C., Emmermann, R., 1986. Hydrothermal alteration of a 1 km
946 section through the upper oceanic crust, Deep Sea Drilling Project Hole 504B:
947 Mineralogy, chemistry and evolution of seawater-basalt interactions. J. Geophys. Res. 91,
948 309-335.
949 Alt, J.C., Teagle, D.A.H., 2003. Hydrothermal alteration of upper oceanic crust formed at a fast-
950 spreading ridge: mineral, chemical, and isotopic evidence from ODP Site 801. Chem.
951 Geol. 201, 191-211.
952 Amonette, J.E., 1994. Quantitative methods in soil mineralogy. Soil Science Society of America,
953 Madison.
954 Andrews, A.J., 1980. Saponite and celadonite in layer 2 basalts, DSDP Leg 37. Contrib. Mineral.
955 Petrol. 73, 323-340.
956 Andrews, A.J., Dollase, W.A., Fleet, M.E., 1983. A Mössbauer study of saponite in layer 2
957 basalt, Deep Sea Drilling Project Leg 69. Initial Rep. Deep Sea Drill. Project 69, 585-
958 588.

April, R.H., Keller, D.M., 1992. Saponite and vermiculite in amygdales of the Granby Basaltic Tuff, Connecticut Valley. Clays Clay Miner. 40, 22-31.
Babechuk, M.G., Weimar, N.E., Kleinhanns, I.C., Eroglu, S., Swanner, E.D., Kenny, G.G., Kamber, B.S., Schoenberg, R., 2019. Pervasively anoxic surface conditions at the onset of the Great Oxidation Event: New multi-proxy constraints from the Cooper Lake paleosol. Precambrian Res. 323, 126-163.
Badaut, D., Besson, G., Decarreau, A., Rautureau, R., 1985. Occurrence of a ferrous, trioctahedral smectite in Recent sediments of Atlantis II Deep, Red Sea. Clay Miner. 20, 389-404.
Baldermann, A., Dohrmann, R., Kaufhold, S., Nickel, C., Letofsky-Papst, I., Dietzel, M., 2014. The Fe-Mg-saponite solid solution series–a hydrothermal synthesis study. Clay Miner. 49, 391-415.
Ballet, O., Coey, J.M.D., Burke, K.J., 1985. Magnetic properties of sheet silicates; 2:1:1 layer minerals. Phys. Chem. Miner. 12, 370-378.
Baron, F., Petit, S., Pentrák, M., Decarreau, A., Stucki, J.W., 2017. Revisiting the nontronite Mössbauer spectra. Am. Mineral. 102, 1501-1515.
Benzine, J., Shelobolina, E., Xiong, M.Y., Kennedy, D.W., McKinley, J.P., Lin, X.J., Roden, E.E., 2013. Fe-phyllosilicate redox cycling organisms from a redox transition zone in Hanford 300 Area sediments. Front. Microbiol. 4, 388.
Betlach, M.R., Tiedje, J.M., 1981. Kinetic explanation for accumulation of nitrite, nitric oxide, and nitrous oxide during bacterial denitrification. Appl. Environ. Microbiol. 42, 1074-1084.
Brindley, G.W., Brown, G., 1982. Crystal structures of clay minerals and their X-ray identification. Mineralogical Society, London.
Byrne, J.M., Klueglein, N., Pearce, C., Rosso, K.M., Appel, E., Kappler, A., 2015. Redox cycling of Fe(II) and Fe(III) in magnetite by Fe-metabolizing bacteria. Science 347, 1473-1476.
Canfield, D.E., 2005. The early history of atmospheric oxygen: homage to Robert M. Garrels. Annu. Rev. Earth Planet. Sci. 33, 1-36.
Canfield, D.E., Poulton, S.W., Narbonne, G.M., 2007. Late-Neoproterozoic deep-ocean oxygenation and the rise of animal life. Science 315, 92-95.
Cardile, C.M., Johnston, J.H., Dickson, D.P.E., 1986. Magnetic Ordering At 4.2 And 1.3 K in Nontronites of Different Iron Contents: A ^{57}Fe Mössbauer Spectroscopic Study. Clays Clay Miner. 34, 233-238.
Chemtob, S.M., Nickerson, R.D., Morris, R.V., Agresti, D.G., Catalano, J.G., 2015. Synthesis and structural characterization of ferrous trioctahedral smectites: Implications for clay mineral genesis and detectability on Mars. J. Geophys. Res.: Planets 120, 1119-1140.
Chemtob, S.M., Nickerson, R.D., Morris, R.V., Agresti, D.G., Catalano, J.G., 2017. Oxidative alteration of ferrous smectites and implications for the redox evolution of early Mars. J. Geophys. Res.: Planets 122, 2469-2488.
Chen, C., Kukkadapu, R.K., Lazareva, O., Sparks, D.L., 2017. Solid-phase Fe speciation along the vertical redox gradients in floodplains using XAS and Mössbauer spectroscopies. Environ. Sci. Technol. 51, 7903-7912.
Chen, C., Meile, C., Wilmoth, J., Barcellos, D., Thompson, A., 2018. Influence of pO_2 on iron redox cycling and anaerobic organic carbon mineralization in a humid tropical forest soil. Environ. Sci. Technol. 52, 7709-7719.

1005 Colwell, F.S., D'Hondt, S., 2013. Nature and extent of the deep biosphere. Rev. Mineral.
1006 Geochem. 75, 547-574.
1007 Craw, D., Smith, D.W., Youngson, J.H., 1995. Formation of authigenic Fe^{2+}-bearing smectite-
1008 vermiculite during terrestrial diagenesis, southern New Zealand. N. Z. J. Geol. Geophys.
1009 38, 151-158.
1010 Decarreau, A., Bonnin, D., 1986. Synthesis and crystallogenesis at low-temperature of Fe(III)-
1011 smectites by evolution of coprecipitated gels - experiments in partially reducing
1012 conditions. Clay Miner. 21, 861-877.
1013 Dong, H., Huang, L., Zhao, L., Zeng, Q., Liu, X., Sheng, Y., Shi, L., Wu, G., Jiang, H., Li, F.,
1014 Zhang, L., Guo, D., Li, G., Hou, W., Chen, H., 2022. A critical review of mineral–
1015 microbe interaction and co-evolution: mechanisms and applications. Natl. Sci. Rev. 9,
1016 nwac128.
1017 Dong, H., Jaisi, D.P., Kim, J., Zhang, G., 2009. Microbe-clay mineral interactions. Am. Mineral.
1018 94, 1505-1519.
1019 Drits, V.A., Manceau, A., 2000. A model for the mechanism of Fe^{3+} to Fe^{2+} reduction in
1020 dioctahedral smectites. Clays Clay Miner. 48, 185-195.
1021 Dyar, M.D., Schaefer, M.W., Sklute, E.C., Bishop, J.L., 2008. Mössbauer spectroscopy of
1022 phyllosilicates: Effects of fitting models on recoil-free fractions and redox ratios. Clay
1023 Miner. 43, 3-33.
1024 Ehlmann, B.L., Hodyss, R., Bristow, T.F., Rossman, G.R., Ammannito, E., De Sanctis, M.C.,
1025 Raymond, C.A., 2018. Ambient and cold-temperature infrared spectra and XRD patterns
1026 of ammoniated phyllosilicates and carbonaceous chondrite meteorites relevant to Ceres
1027 and other solar system bodies. Meteorit. Planet. Sci. 53, 1884-1901.
1028 Emerson, D., Floyd, M.M., 2005. Enrichment and isolation of iron-oxidizing bacteria at neutral
1029 pH, in: Leadbetter, J.R. (Ed.) Methods in Enzymology, Volume 397. Academic Press, pp.
1030 112-123.
1031 Evans, R.J., Rancourt, D.G., Grodzicki, M., 2005. Hyperfine electric field gradients and local
1032 distortion environments of octahedrally coordinated Fe^{2+}. Am. Mineral. 90, 187-198.
1033 Fialips, C.I., Huo, D., Yan, L.B., Wu, J., Stucki, J.W., 2002a. Infrared study of reduced and
1034 reduced-reoxidized ferruginous smectite. Clays Clay Miner. 50, 455-469.
1035 Fialips, C.I., Huo, D.F., Yan, L.B., Wu, J., Stucki, J.W., 2002b. Effect of Fe oxidation state on
1036 the IR spectra of Garfield nontronite. Am. Mineral. 87, 630-641.
1037 Fox, V.K., Kupper, R.J., Ehlmann, B.L., Catalano, J.G., Razzell-Hollis, J., Abbey, W.J., Schild,
1038 D.J., Nickerson, R.D., Peters, J.C., Katz, S.M., 2021. Synthesis and characterization of
1039 Fe(III)-Fe(II)-Mg-Al smectite solid solutions and implications for planetary science. Am.
1040 Mineral. 106, 964-982.
1041 Glass, C., Silverstein, J., 1998. Denitrification kinetics of high nitrate concentration water: pH
1042 effect on inhibition and nitrite accumulation. Water Res. 32, 831-839.
1043 Gorski, C.A., Klüpfel, L.E., Voegelin, A., Sander, M., Hofstetter, T.B., 2012. Redox properties
1044 of structural Fe in clay minerals. 2. Electrochemical and spectroscopic characterization of
1045 electron transfer irreversibility in ferruginous smectite, SWa-1. Environ. Sci. Technol. 46,
1046 9369-9377.
1047 Gorski, C.A., Klüpfel, L.E., Voegelin, A., Sander, M., Hofstetter, T.B., 2013. Redox properties
1048 of structural Fe in clay minerals. 3. Relationships between smectite redox and structural
1049 properties. Environ. Sci. Technol. 47, 13477-13485.

Grabb, K.C., Buchwald, C., Hansel, C.M., Wankel, S.D., 2017. A dual nitrite isotopic investigation of chemodenitrification by mineral-associated Fe(II) and its production of nitrous oxide. Geochim. Cosmochim. Acta 196, 388-402.
Hao, J., Sverjensky, D.A., Hazen, R.M., 2017. A model for late Archean chemical weathering and world average river water. Earth Planet. Sci. Lett. 457, 191-203.
Heller-Kallai, L., Rozenson, I., 1981. The use of Mössbauer spectroscopy of iron in clay mineralogy. Phys. Chem. Miner. 7, 223-238.
Holland, H.D., 2004. 6.21: The geologic history of seawater, in: Elderfield, H. (Ed.) Treatise on Geochemistry. Pergamon, Oxford, pp. 583-685.
Huggins, F.E., 1976. Mössbauer studies of iron minerals under pressures of up to 200 kilobars, in: Strens, R.G.J. (Ed.) The Physics and Chemistry of Minerals and Rocks. Wiley, New York, pp. 613-640.
Ivanov, V.M., 2004. The 125th Anniversary of the Griess Reagent. J. Anal. Chem. 59, 1002-1005.
Jaisi, D.P., Eberl, D.D., Dong, H.L., Kim, J., 2011. The formation of illite from nontronite by mesophilic and thermophilic bacterial reaction. Clays Clay Miner. 59, 21-33.
Kappler, A., Schink, B., Newman, D.K., 2005. Fe(III) mineral formation and cell encrustation by the nitrate-dependent Fe(II)-oxidizer strain BoFeN1. Geobiology 3, 235-245.
Khaled, E.M., Stucki, J.W., 1991. Iron oxidation state effects on cation fixation in smectites. Soil Sci. Soc. Am. J. 55, 550-554.
Kim, J., Dong, H.L., Seabaugh, J., Newell, S.W., Eberl, D.D., 2004. Role of microbes in the smectite-to-illite reaction. Science 303, 830-832.
Klueglein, N., Kappler, A., 2013. Abiotic oxidation of Fe(II) by reactive nitrogen species in cultures of the nitrate-reducing Fe(II) oxidizer *Acidovorax* sp BoFeN1 - questioning the existence of enzymatic Fe(II) oxidation. Geobiology 11, 180-190.
Klueglein, N., Zeitvogel, F., Stierhof, Y.D., Floetenmeyer, M., Konhauser, K.O., Kappler, A., Obst, M., 2014. Potential role of nitrite for abiotic Fe(II) oxidation and cell encrustation during nitrate reduction by denitrifying bacteria. Appl. Environ. Microbiol. 80, 1051-1061.
Kohyama, N., Shimoda, S., Sudo, T., 1973. Iron-rich saponite (ferrous and ferric forms). Clays Clay Miner. 21, 229-237.
Komadel, P., Lear, P.R., Stucki, J.W., 1990. Reduction and reoxidation of nontronite: Extent of reduction and reaction rates. Clays Clay Miner. 38, 203-208.
Komadel, P., Madejová, J., Bujdák, J., 2005. Preparation and properties of reduced-charge smectites – A review. Clays Clay Miner. 53, 313-334.
Komadel, P., Madejova, J., Stucki, J.W., 1995. Reduction and reoxidation of nontronite: Questions of reversibility. Clays Clay Miner. 43, 105-110.
Komadel, P., Madejova, J., Stucki, J.W., 1999. Partial stabilization of Fe(II) in reduced ferruginous smectite by Li fixation. Clays Clay Miner. 47, 458-465.
Koo, T.-H., Jang, Y.-N., Kogure, T., Kim, J.H., Park, B.C., Sunwoo, D., Kim, J.-W., 2014. Structural and chemical modification of nontronite associated with microbial Fe(III) reduction: Indicators of “illitization”. Chem. Geol. 377, 87-95.
Kristmannsdottir, H., 1979. Alteration of basaltic rocks by hydrothermal-activity at 100-300°C, in: Mortland, M.M., Farmer, V.C. (Eds.), International Clay Conference 1978. Elsevier, Amsterdam, pp. 359-367.

Lagarec, K., Rancourt, D.G., 1997. Extended Voigt-based analytic lineshape method for determining N-dimensional correlated hyperfine parameter distributions in Mössbauer spectroscopy. Nucl. Instrum. Methods Phys. Res., Sect. B 129, 266-280.

Luan, F., Gorski, C.A., Burgos, W.D., 2014. Thermodynamic controls on the microbial reduction of iron-bearing nontronite and uranium. Environ. Sci. Technol. 48, 2750-2758.

Lyons, T.W., Reinhard, C.T., Planavsky, N.J., 2014. The rise of oxygen in Earth's early ocean and atmosphere. Nature 506, 307-315.

Manceau, A., Drits, V.A., Lanson, B., Chateigner, D., Wu, J., Huo, D., Gates, W.P., Stucki, J.W., 2000a. Oxidation-reduction mechanism of iron in dioctahedral smectites: II. Crystal chemistry of reduced Garfield nontronite. Am. Mineral. 85, 153-172.

Manceau, A., Lanson, B., Drits, V.A., Chateigner, D., Gates, W.P., Wu, J., Huo, D., Stucki, J.W., 2000b. Oxidation-reduction mechanism of iron in dioctahedral smectites: I. Crystal chemistry of oxidized reference nontronites. Am. Mineral. 85, 133-152.

Moore, D.M., Reynolds, R.C., 1997. X-Ray Diffraction and the Identification and Analysis of Clay Minerals, 2nd ed. Oxford University Press, New York.

Murad, E., Cashion, J., 2004. Mössbauer Spectroscopy of Environmental Materials and Their Industrial Utilization Kluwer Academic Publishers, Norwell, Massachusetts.

Neumann, A., Hofstetter, T.B., Lussi, M., Cirpka, O.A., Petit, S., Schwarzenbach, R.P., 2008. Assessing the redox reactivity of structural iron in smectites using nitroaromatic compounds as kinetic probes. Environ. Sci. Technol. 42, 8381-8387.

Neumann, A., Petit, S., Hofstetter, T.B., 2011. Evaluation of redox-active iron sites in smectites using middle and near infrared spectroscopy. Geochim. Cosmochim. Acta 75, 2336-2355.

Neveu, M., Desch, S.J., Castillo-Rogez, J.C., 2017. Aqueous geochemistry in icy world interiors: Equilibrium fluid, rock, and gas compositions, and fate of antifreezes and radionuclides. Geochim. Cosmochim. Acta 212, 324-371.

Newville, M., 2001. IFEFFIT : interactive XAFS analysis and FEFF fitting. Journal of Synchrotron Radiation 8, 322-324.

Noor, N., Thompson, A., 2022. Localized alteration of ferrihydrite natural organic matter coprecipitates following reaction with Fe(II). Soil Sci. Soc. Am. J. 86, 253-263.

Parthasarathy, G., Choudary, B.M., Sreedhar, B., Kunwar, A.C., Srinivasan, R., 2003. Ferrous saponite from the Deccan Trap, India, and its application in adsorption and reduction of hexavalent chromium. Am. Mineral. 88, 1983-1988.

Pentráková, L., Su, K., Pentrák, M., Stucki, J.W., 2013. A review of microbial redox interactions with structural Fe in clay minerals. Clay Miner. 48, 543-560.

Rancourt, D.G., 1994a. Mössbauer spectroscopy of minerals II. Problem of resolving cis and trans octahedral Fe^{2+} sites. Phys. Chem. Miner. 21, 250-257.

Rancourt, D.G., 1994b. Mössbauer spectroscopy of minerals: I. Inadequacy of Lorentzian-line doublets in fitting spectra arising from quadrupole splitting distributions. Phys. Chem. Miner. 21, 244-249.

Rancourt, D.G., Christie, I.A.D., Lamarche, G., Swainson, I., Flandrois, S., 1994. Magnetism of synthetic and natural annite mica: ground state and nature of excitations in an exchange-wise two-dimensional easy-plane ferromagnet with disorder. J. Magn. Magn. Mater. 138, 31-44.

Ravel, B., Newville, M., 2005. ATHENA, ARTEMIS, HEPHAESTUS: data analysis for X-ray absorption spectroscopy using IFEFFIT. Journal of Synchrotron Radiation 12, 537-541.

Redhammer, G.n.J., Roth, G., 2002. Single-crystal structure refinements and crystal chemistry of synthetic trioctahedral micas $KM_3(Al^{3+},Si^{4+})_4O_{10}(OH)_2$, where M = Ni^{2+}, Mg^{2+}, Co^{2+}, Fe^{2+}, or Al^{3+}. Am. Mineral. 87, 1464-1476.

Ribeiro, F.R., Fabris, J.D., Kostka, J.E., Komadel, P., Stucki, J.W., 2009. Comparisons of structural iron reduction in smectites by bacteria and dithionite: II. A variable-temperature Mössbauer spectroscopic study of Garfield nontronite. Pure Appl. Chem. 81, 1499-1509.

Riding, R., Fralick, P., Liang, L., 2014. Identification of an Archean marine oxygen oasis. Precambrian Res. 251, 232-237.

Rivkin, A.S., Volquardsen, E.L., Clark, B.E., 2006. The surface composition of Ceres: Discovery of carbonates and iron-rich clays. Icarus 185, 563-567.

Rothwell, K.A., 2019. From the lab to the real world: The redox reactivity of Fe-bearing clay minerals in complex biogeochemical environments. Newcastle University, Newcastle, UK, p. 156.

Sakuma, H., Morida, K., Takahashi, Y., Fukushi, K., Noda, N., Sekine, Y., Tamura, K., 2022. Synthesis of ferrian and ferro-saponites: Implications for the structure of (Fe,Mg)-smectites formed under reduced conditions. Am. Mineral. 107, 1926-1935.

Shannon, R.D., 1976. Revised effective ionic radii and systematic studies of interatomic distances in halides and chalcogenides. Acta Crystallogr. A32, 751-767.

Shelobolina, E.S., Konishi, H., Xu, H., Benzine, J., Xiong, M.Y., Wu, T., Blöthe, M., Roden, E., 2012a. Isolation of phyllosilicate-iron redox cycling microorganisms from an illite-smectite rich hydromorphic soil. Front. Microbiol. 3, 134.

Shelobolina, E.S., Vanpraagh, C.G., Lovley, D.R., 2003. Use of ferric and ferrous iron containing minerals for respiration by *Desulfitobacterium frappieri*. Geomicrobiol. J. 20, 143-156.

Shelobolina, E.S., Xu, H., Konishi, H., Kukkadapu, R., Wu, T., Blöthe, M., Roden, E., 2012b. Microbial lithotrophic oxidation of structural Fe(II) in biotite. Appl. Environ. Microbiol. 78, 5746-5752.

Shen, S., Stucki, J.W., 1994. Effects of iron oxidation state on the fate and behavior of potassium in soils, in: Havlin, J.L., Jacobsen, J.S. (Eds.), Soil Testing: Prospects for Improving Nutrient Recommendations. Soil Science Society of America and American Society of Agronomy, Madison, pp. 173-185.

Shen, S.Y., Stucki, J.W., Boast, C.W., 1992. Effects of structural iron reduction on the hydraulic conductivity of Na-smectite. Clays Clay Miner. 40, 381-386.

Shen, Y., Canfield, D.E., Knoll, A.H., 2002. Middle Proterozoic ocean chemistry: Evidence from the McArthur Basin, northern Australia. Am. J. Sci. 302, 81-109.

Stucki, J.W., 2011. A review of the effects of iron redox cycles on smectite properties. C.R. Geosci. 343, 199-209.

Sun, J., Mailloux, B.J., Chillrud, S.N., van Geen, A., Thompson, A., Bostick, B.C., 2018. Simultaneously quantifying ferrihydrite and goethite in natural sediments using the method of standard additions with X-ray absorption spectroscopy. Chem. Geol. 476, 248-259.

Tarafder, P.K., Thakur, R., 2013. An optimised 1,10-phenanthroline method for the determination of ferrous and ferric oxides in silicate rocks, soils and minerals. Geostand. Geoanal. Res. 37, 155-168.

Teagle, D.A.H., Alt, J.C., Bach, W., Halliday, A.N., Erzinger, J., 1996. Alteration of upper ocean crust in a ridge-flank hydrothermal upflow zone: Mineral, chemical, and isotopic constraints from Hole 896A. Proc. Ocean Drill. Program Part B Sci. Results 148, 119-150.

Treiman, A.H., Morris, R.V., Agresti, D.G., Graff, T.G., Achilles, C.N., Rampe, E.B., Bristow, T.F., Ming, D.W., Blake, D.F., Vaniman, D.T., 2014. Ferrian saponite from the Santa Monica Mountains (California, USA, Earth): Characterization as an analog for clay minerals on Mars with application to Yellowknife Bay in Gale Crater. Am. Mineral. 99, 2234-2250.

Vaniman, D.T., Bish, D.L., Ming, D.W., Bristow, T.F., Morris, R.V., Blake, D.F., Chipera, S.J., Morrison, S.M., Treiman, A.H., Rampe, E.B., Rice, M., Achilles, C.N., Grotzinger, J.P., McLennan, S.M., Williams, J., Bell, J.F., Newsom, H.E., Downs, R.T., Maurice, S., Sarrazin, P., Yen, A.S., Morookian, J.M., Farmer, J.D., Stack, K., Milliken, R.E., Ehlmann, B.L., Sumner, D.Y., Berger, G., Crisp, J.A., Hurowitz, J.A., Anderson, R., Des Marais, D.J., Stolper, E.M., Edgett, K.S., Gupta, S., Spanovich, N., Team, M.S.L.S., 2014. Mineralogy of a mudstone at Yellowknife Bay, Gale crater, Mars. Science 343, 1243480.

Vantelon, D., Montarges-Pelletier, E., Michot, L.J., Pelletier, M., Thomas, F., Briois, V., 2003. Iron distribution in the octahedral sheet of dioctahedral smectites. An Fe K-edge X-ray absorption spectroscopy study. Phys. Chem. Miner. 30, 44-53.

Vantelon, D., Pelletier, M., Michot, L.J., Barres, O., Thomas, F., 2001. Fe, Mg and Al distribution in the octahedral sheet of montmorillonites. An infrared study in the OH^- bending region. Clay Miner. 36, 369-379.

Velde, B., Meunier, A., 2008. The Origin of Clay Minerals in Soils and Weathered Rocks. Springer, Berlin, Heidelberg.

Watanabe, T., Sato, T., 1988. Expansion characteristics of montmorillonite and saponite under various relative humidity conditions. Clay Sci. 7, 129-138.

Webb, S.M., 2005. SIXpack: a graphical user interface for XAS analysis using IFEFFIT. Physica Scripta 2005, 1011.

Weber, K.A., Pollock, J., Cole, K.A., O'Connor, S.M., Achenbach, L.A., Coates, J.D., 2006. Anaerobic nitrate-dependent iron(II) bio-oxidation by a novel lithoautotrophic betaproteobacterium, strain 2002. Appl. Environ. Microbiol. 72, 686-694.

Whitaker, A.H., Austin, R.E., Holden, K.L., Jones, J.L., Michel, F.M., Peak, D., Thompson, A., Duckworth, O.W., 2021. The structure of natural biogenic iron (oxyhydr)oxides formed in circumneutral pH environments. Geochim. Cosmochim. Acta 308, 237-255.

Zhao, L., Dong, H., Kukkadapu, R.K., Zeng, Q., Edelmann, R.E., Pentrák, M., Agrawal, A., 2015. Biological redox cycling of iron in nontronite and its potential application in nitrate removal. Environ. Sci. Technol. 49, 5493-5501.

Zhao, L.D., Dong, H.L., Kukkadapu, R., Agrawal, A., Liu, D., Zhang, J., Edelmann, R.E., 2013. Biological oxidation of Fe(II) in reduced nontronite coupled with nitrate reduction by *Pseudogulbenkiania* sp. strain 2002. Geochim. Cosmochim. Acta 119, 231-247.

Zhou, N., Kupper, R.J., Catalano, J.G., Thompson, A., Chan, C.S., 2022. Biological oxidation of Fe(II)-bearing smectite by microaerophilic Fe-oxidizer *Sideroxydans lithotrophicus* using dual Cyc2 and Mto Fe oxidation pathways. Environ. Sci. Technol. 56, 17443–17453.

Table 1. Concentrations and volumes of each salt used in the initial precipitating solutions for the synthesis of the smectites used in this study.

Designation	Target Fe:Mg:Al mole ratio	Final Fe:Mg:Al mole ratio	1 mol L^{-1} $FeCl_2$	1 mol L^{-1} $MgCl_2$	1 mol L^{-1} $AlCl_3$	0.5 mol L^{-1} Na_2SiO_3
Moderate-Iron	40:40:20	53:24:23	10 mL	10 mL	5 mL	58.67 mL
High-Iron	60:20:20	70:08:23	15 mL	5 mL	5 mL	58.67 mL

1233 **Table 2**. Structural formulae for the synthetic smectites used in this study.

Label	Formula	Octahedral Occupancy	Fe(II) / Fe(Total)	Total Charge	O-Charge	T-Charge
Moderate-Iron	$Ca_{0.17}(Fe^{II}_{1.59}Mg_{0.78}Fe^{III}_{0.12}Al_{0.33})(Si_{3.58}Al_{0.42})O_{10}(OH)_2$	2.82	0.94	-0.34	+0.08	-0.42
High-Iron	$Ca_{0.20}(Fe^{II}_{2.16}Mg_{0.26}Fe^{III}_{0.19}Al_{0.24})(Si_{3.48}Al_{0.52})O_{10}(OH)_2$	2.85	0.92	-0.40	+0.13	-0.52

1234

Table 3. Fitting parameters of the 295 K Mössbauer spectra of the smectites before and after oxidant exposure.

Smectite	Component	CS (mm/s) [a]	QS (mm/s) [b]	Area (%)
Moderate-Iron				
	Ferric	0.45±0.03	0.40±0.05	8.1±0.8%
	Ferrous	1.130±0.003	2.614±0.005	92.0± 0.8%
High-Iron				
	Ferric	0.50±0.02	0.41±0.02	8.4±0.3%
	Ferrous	1.134±0.001	2.54±0.03	91.6±0.3%
Moderate-iron nitrite				
	Ferric	0.488±0.009	0.49±0.03	24.1±0.3%
	Ferrous	1.131±0.001	2.592±0.002	75.9±0.3%
High-iron nitrite				
	Ferric	0.43±0.01	0.79±0.02	49.0±0.6%
	Ferrous	1.120±0.006	2.53±0.01	51.0±0.6%
Moderate-iron 2% O_2				
	Ferric	0.37±0.01	0.80±0.02	57.7±0.7%
	Ferrous	1.122±0.002	2.56±0.02	42.3±0.7%
High-iron 2% O_2				
	Ferric	0.37±0.05	0.81±0.01	79.9±0.8%
	Ferrous	1.06±0.03	2.45±0.06	20.1±0.8%
Moderate-iron 21% O_2				
	Ferric	0.36±0.09	0.87±0.02	71.5±0.6%
	Ferrous	1.13±0.01	2.51±0.03	28.5±0.6%
High-iron 21% O_2				
	Ferric	0.353±0.008	0.85±0.01	86.0±0.6%
	Ferrous	1.13±0.04	2.33±0.07	14.0±0.6%
Moderate-iron H_2O_2				
	Ferric	0.351±0.003	0.996±0.005	93.7±0.4%
	Ferrous	1.14±0.02	2.42±0.03	6.3±0.4%
High-iron H_2O_2				
	Ferric	0.352±0.008	0.898±0.005	96.6±0.6%
	Ferrous	1.14±0.02	2.30±0.07	3.4±0.6%

[a] Chemical shift.
[b] Quadrupole splitting.

Table 4. Results of individual oxidation experiments.

Smectite	Oxidant	Initial pH	Final pH	Initial Colorimetric Smectite Fe(II)/Fe(Total)	Final Colorimetric Smectite Fe(II)/Fe(Total)	Final Mössbauer Smectite Fe(II)/Fe(Total)
Moderate-Iron	None	6.29±0.01[a]	6.70±0.02	83±3%	88±2%	84.3±0.5%
	21% O_2	6.16±0.01	6.98±0.02	81±1%	26±4%	28.5±0.6%
	2% O_2	6.20± 0.02	6.66±0.05	75±3%	43.4±0.4%	42.3±0.7%
	5 mmol $L^{-1}NO_2^-$	6.29± 0.08	6.73±0.01	85±4%	85±4%	75.9±0.3%
	H_2O_2	6.30± 0.02	-[b]	78±4%	6±3%	6.3±0.4%
High-Iron	None	6.18± 0.01	6.60±0.01	92±3%	93±3%	91.6±0.3%
	21% O_2	6.24± 0.02	7.11±0.02	92.4±0.8%	14.1± 0.2%	14.0±0.6%
	2% O_2	6.25± 0.01	6.68±0.06	89±1%	28.6±0.1%	20.1±0.8%
	5mM NO_2^-	6.26± 0.02	6.57±0.04	90±5%	73±4%	51.0±0.6%
	H_2O_2	6.26± 0.05	-	85±4%	5.3±0.5%	3.4±0.6%

[a] pH and colorimetric Fe(II)/Fe(Total) percentages are the average and standard deviation of measurements from triplicate samples. Mössbauer Fe(II)/Fe(Total) is the uncertainty in the fit of a single sample

[b] pH was not measured following H_2O_2 exposure

Table 5. Kinetic fit parameters for each of the oxygen exposure studies.

Smectite	Oxidant	k_1 (h^{-1}) [a]	a_1	k_2 (h^{-1})	a_2	Recalcitrant Fe(II) Fraction	Reduced χ^2 [b]
Moderate-Iron							
	21% O_2	2.58	0.30±0.02	0.07±0.01	0.29±0.01	0.22±0.02	1.82[b]
	2% O_2	0.47	0.06±0.03	0.10±0.07	0.27±0.01	0.41±0.01	2.10
High-Iron							
	21% O_2	2.6±0.4	0.48±0.02	0.040±0.007	0.36±0.02	0.091±0.009	1.66
	2% O_2	0.5±0.1	0.38±0.03	0.012±0.003	0.36±0.02	0.16±0.02	3.71

[a] Fitting parameters are as follows: k_1 is the rate constant of the first equation, a_1 is the portion of the ferrous iron that is governed by the first rate term, k_2 is the rate constant of the second equation, a_2 is the portion governed by the second rate term, and the recalcitrant fraction is the portion of Fe(II) that is assumed non-reactive by the model. Note the dependent variable being modeled is unitless (mole fraction) and thus does not contribute to the units for the rate constants.

[b] Reduced χ^2 is a goodness of fit parameter.

Table 6. Fitted (001) peak and (06,33) band positions and calculated d-space values.

Smectite	(001) position (°2θ)	d_{001} (Å)	(06,33) position (°2θ)	$d_{06,33}$ (Å)
Moderate-Iron				
Initial	5.45(2)[a]	16.2	60.163(8)	1.537
21% O_2	6.17(2)	14.3	60.509(6)	1.529
2% O_2	6.18(2)	14.3	60.41(1)	1.531
5 mmol L^{-1} NO_2^-	5.86(1)	15.1	60.247(9)	1.535
H_2O_2	6.42(2)	13.8	60.704(6)	1.524
High-Iron				
Initial	5.37(2)	16.4	59.787(5)	1.546
21% O_2	6.40(3)	13.8	60.619(8)	1.526
2% O_2	6.17(2)	14.3	60.434(9)	1.531
5 mmol L^{-1} NO_2^-	5.90(2)	15.0	60.071(6)	1.539
H_2O_2	6.19(2)	14.3	60.811(9)	1.522

[a] Values in parentheses represent the uncertainty in the last digit.

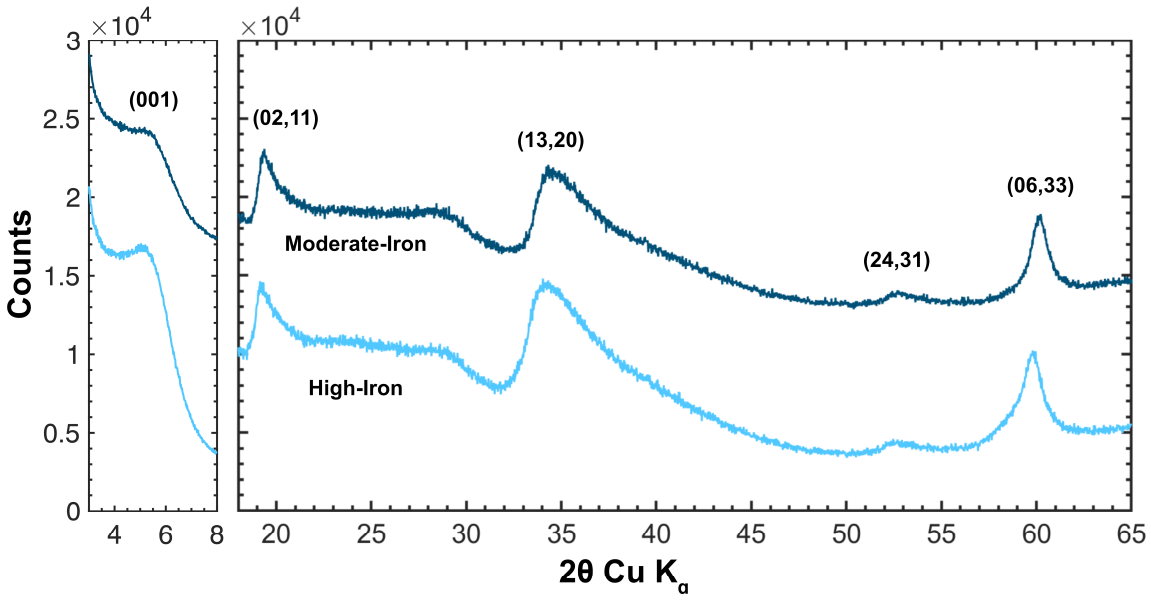

Figure 1. XRD patterns of the initial synthetic smectites. Patterns are offset vertically for clarity. Labels indicate major peaks and bands. Data between 8 and 18° is obscured by a large scattering feature from the acrylic dome used to prevent oxidation and is thus not displayed.

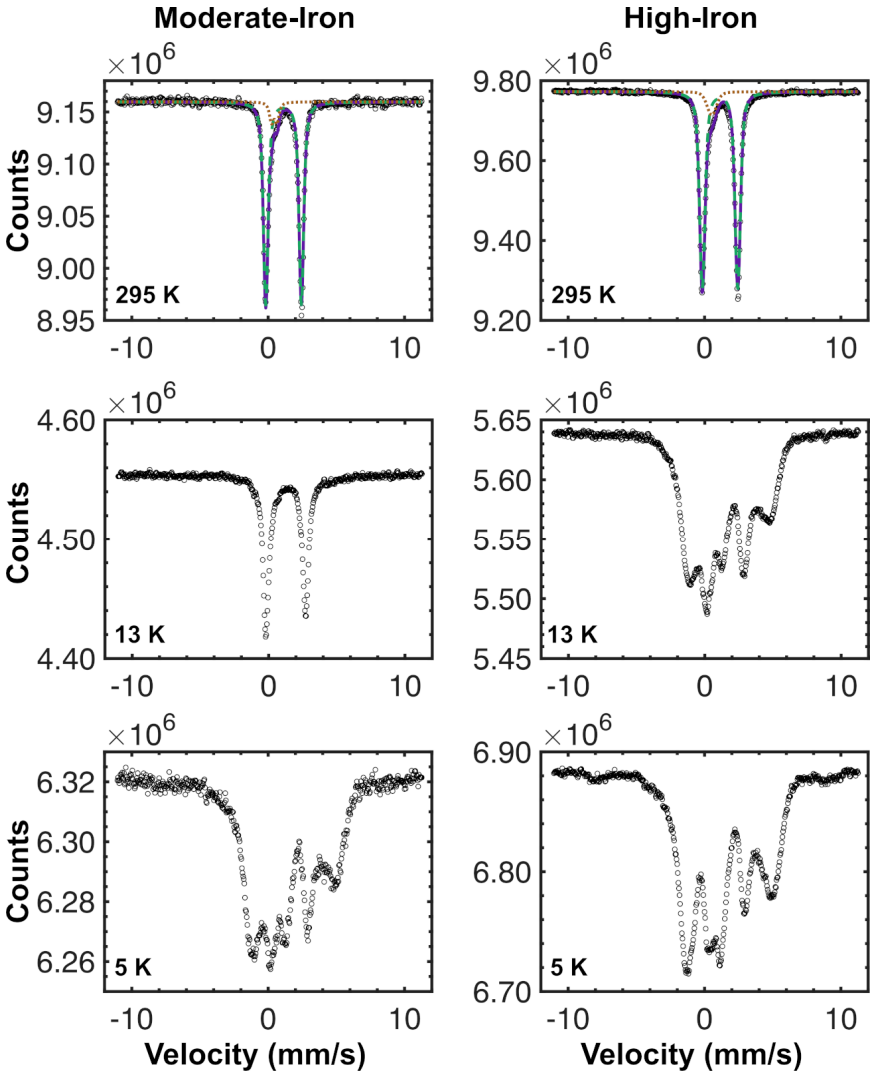

Figure 2. ^{57}Fe Mössbauer spectra of the synthetic smectites. Fits to the 295 K spectra in purple are the sum of ferrous and ferric components represented by dashed green and dotted brown lines, respectively.

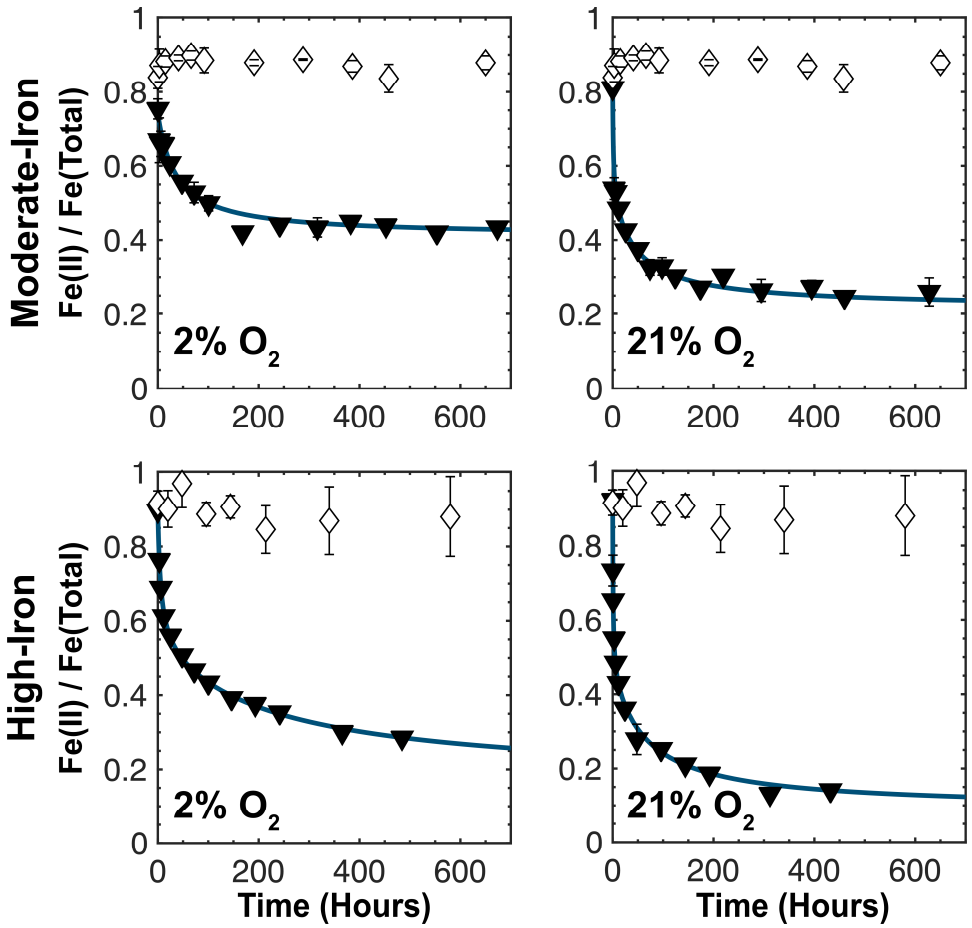

Figure 3. Fe(II)/Fe(Total) and modeled rates of oxidation for both smectite compositions (rows) exposed to oxygen at two different partial pressures (columns) compared with oxidant free control studies. Open diamonds are the oxidant-free control experiments, solid triangles are for the experiments using dissolved oxygen, and blue lines are the kinetic model fits.

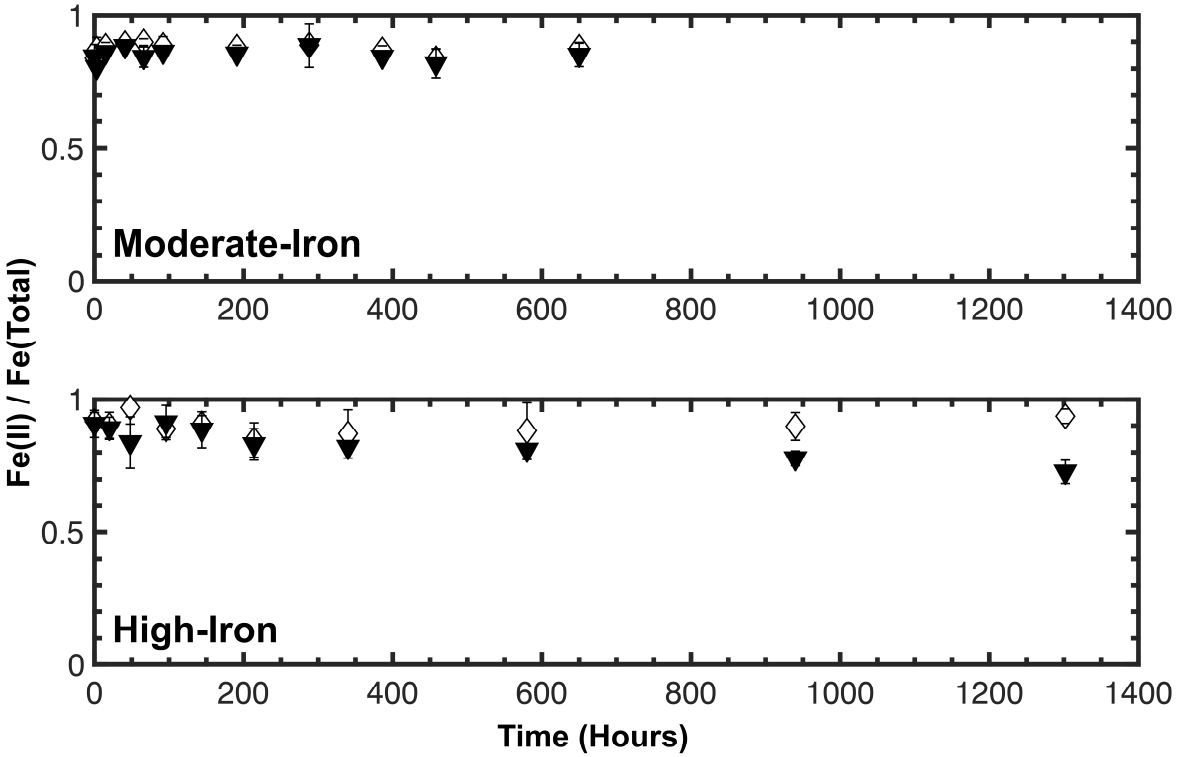

Figure 4. Fe(II)/Fe(Total) for both smectites exposed to 5 mmol L^{-1} nitrite compared with oxidant-free controls.

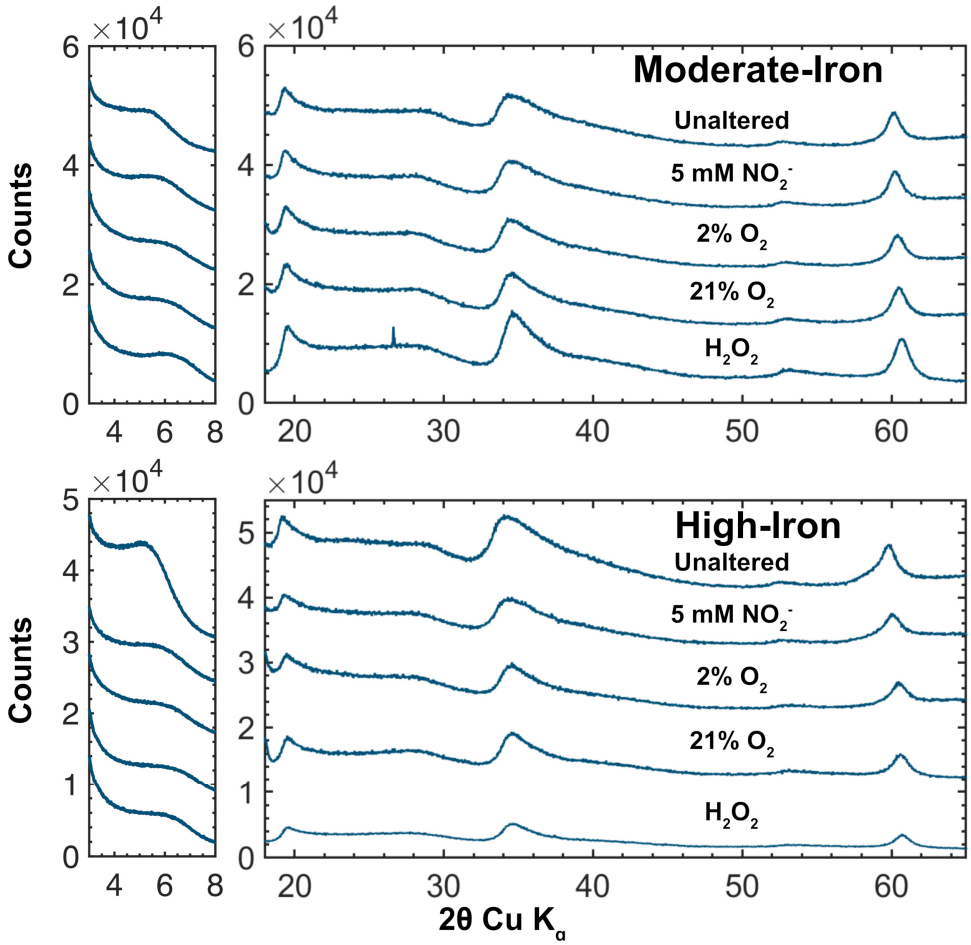

Figure 5. XRD patterns of each smectite and its oxidation products, vertically offset. The small sharp peak in the moderate-iron H_2O_2 pattern is from a quartz contaminant introduced during grinding.

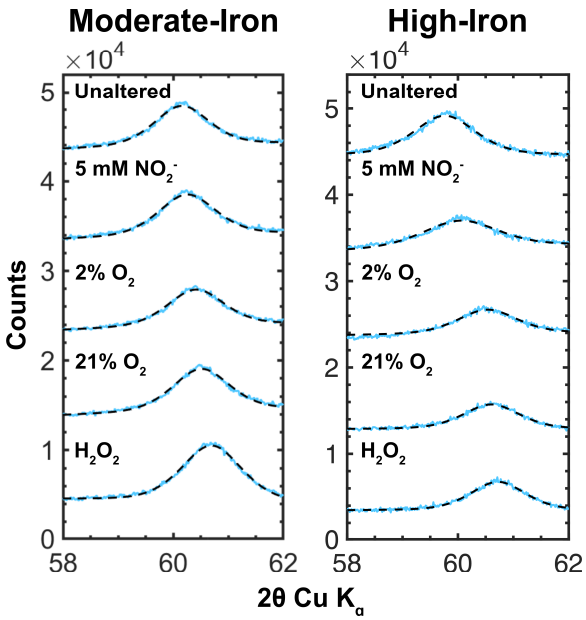

Figure 6. The (06,33) band in the XRD patterns (solid) and fitted peaks (dashed) of each smectite and its oxidation products.

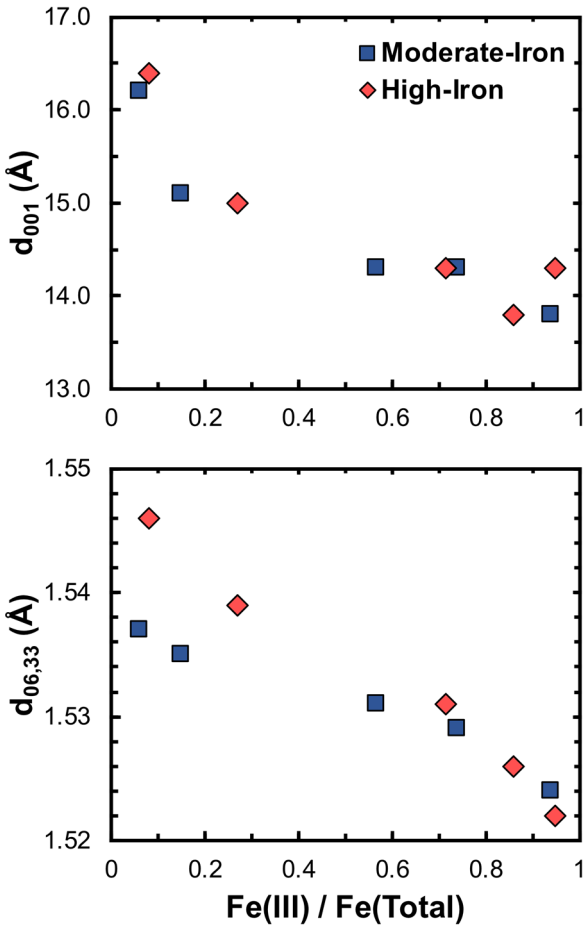

Figure 7. Relationship between the smectite (001) and (06,33) diffraction features and the extent of iron oxidation.

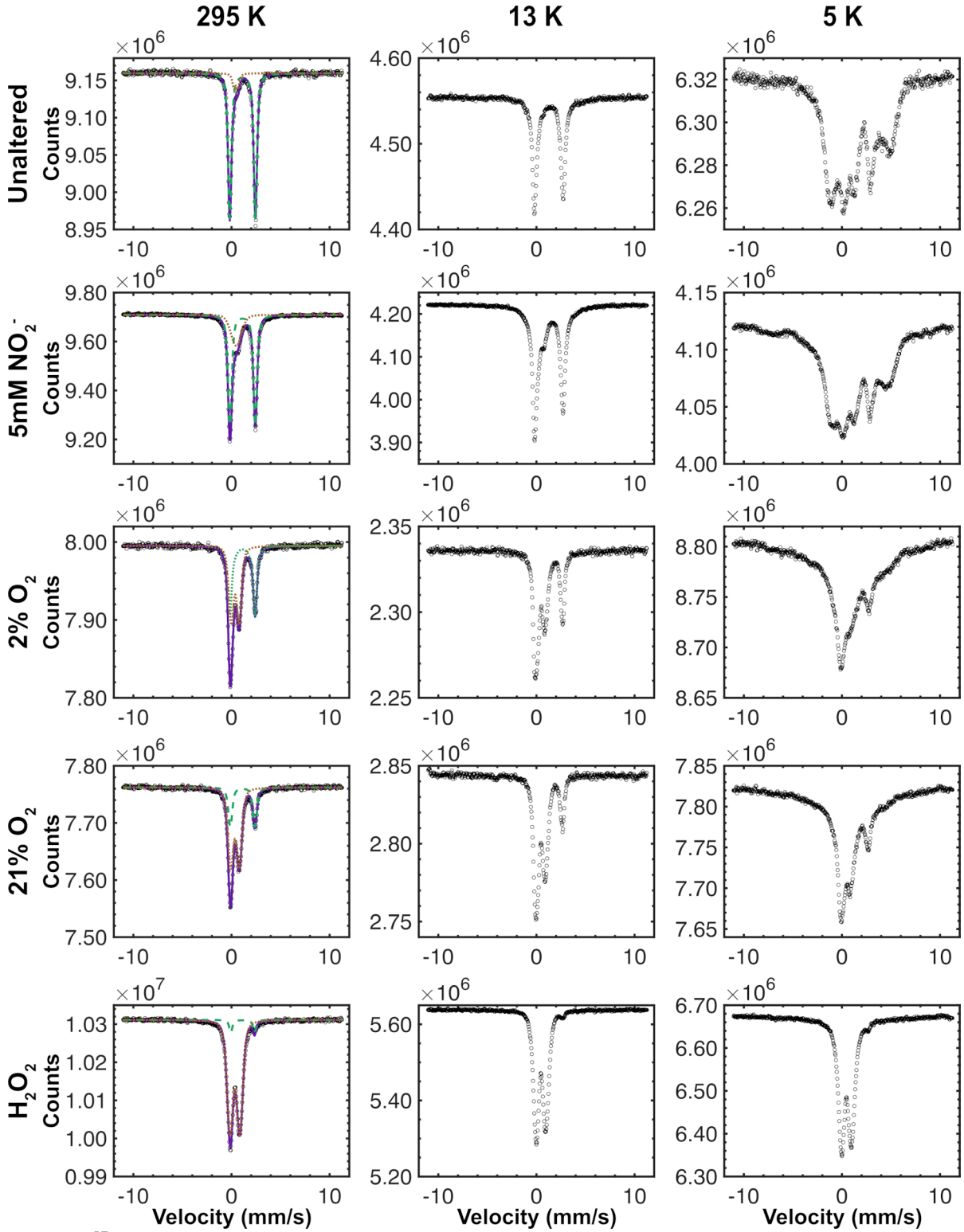

Figure 8. ^{57}Fe Mössbauer spectra of moderate-iron samples from the study, collected at 295 K, 13 K, and 5 K. Fits to the 295 K spectra in purple are the sum of ferrous and ferric components represented by dashed green and dotted brown lines, respectively.

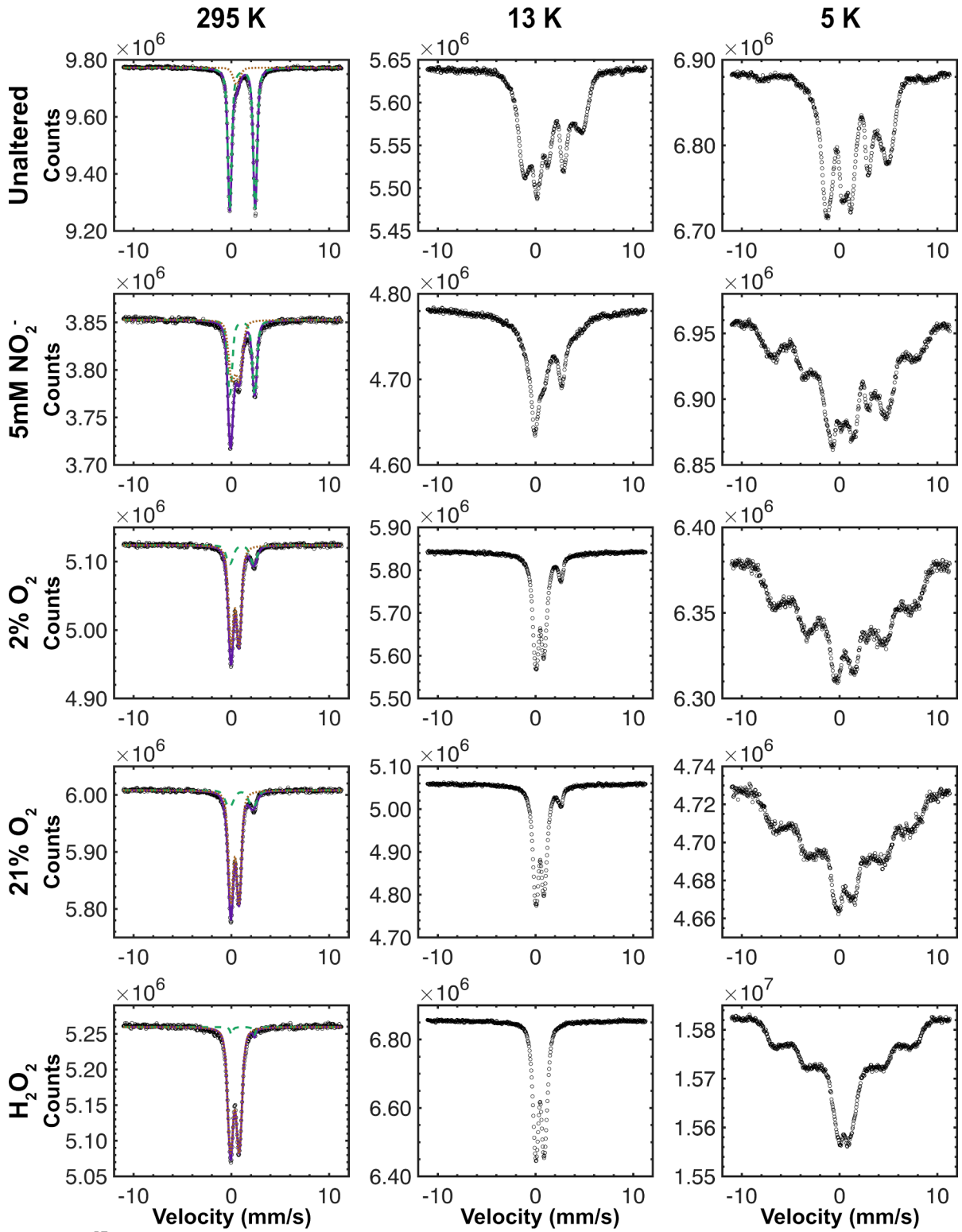

Figure 9. ^{57}Fe Mössbauer spectra of high-iron samples from the study, collected at 295 K, 13 K, and 5 K. Fits to the 295 K spectra in purple are the sum of ferrous and ferric components represented by dashed green and dotted brown lines, respectively.

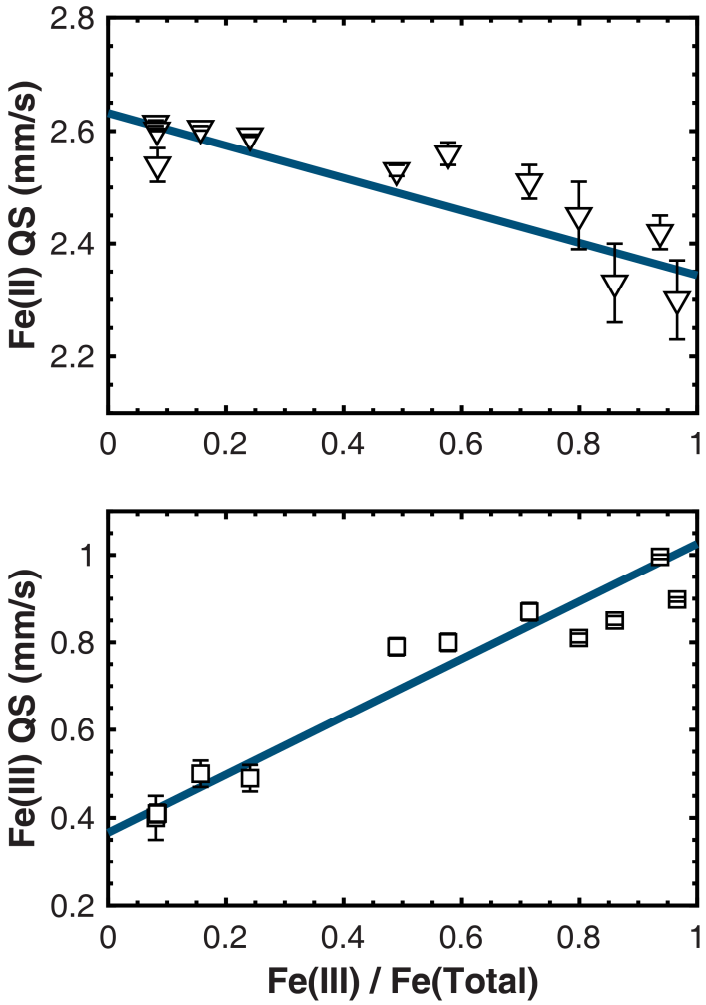

Figure 10. The relationship between the quadrupole shift (QS) of the Fe(II) and Fe(III) doublets in the 295 K ^{57}Fe Mössbauer spectra and the fraction of iron occurring as Fe(III). The lines represent linear regressions weighted by the uncertainties in the QS values.

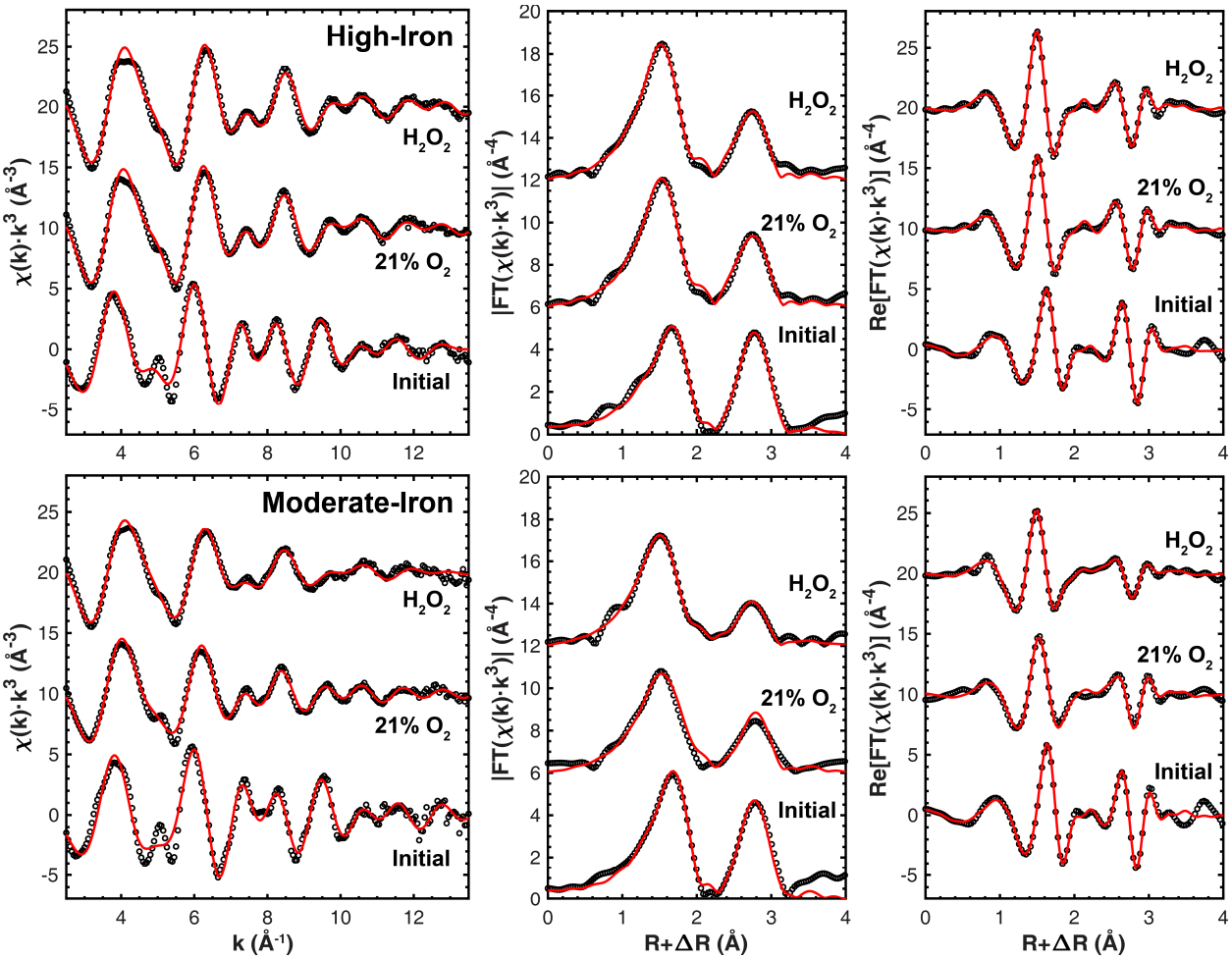

Figure 11. Data (dotted) and structural model fits (solid) of the Fe K-edge EXAFS spectra (left), Fourier transform magnitudes (center), and real components of the Fourier transforms (right) of the synthetic smectites and their oxidation products.

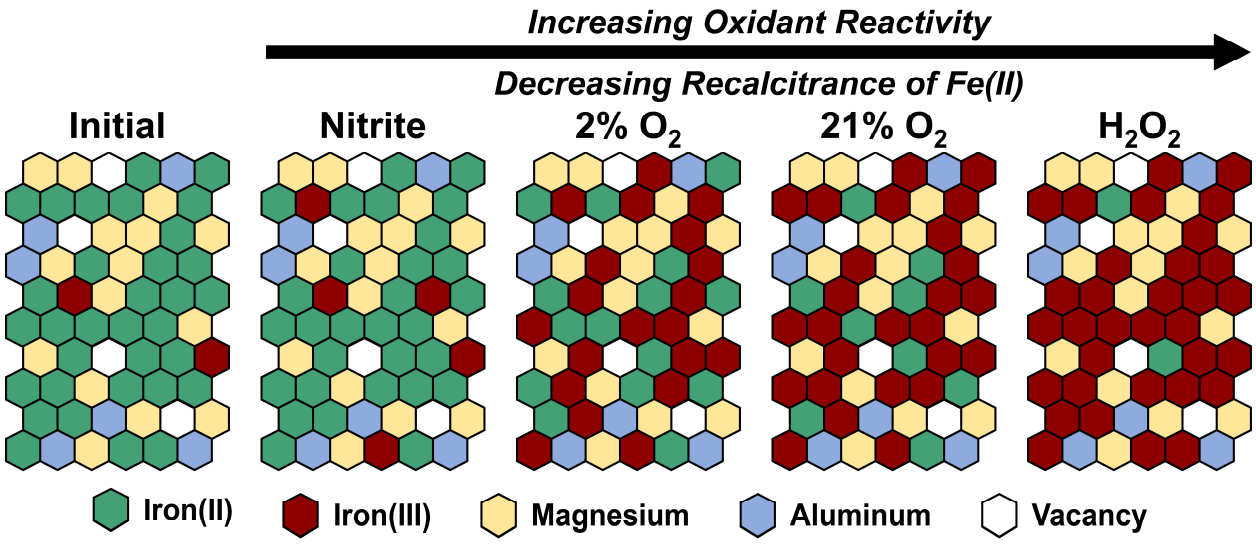

Figure 12. Progressive oxidation in response to oxidants of increasing reactivity creates an array of evolving local coordination environments around iron, with some recalcitrant Fe(II) remaining in the octahedral sheet.

Supplementary Material for

Oxidation Rates and Redox Stabilization of Ferrous Iron in Trioctahedral Smectites

Robert J. Kupper[1], Nanqing Zhou[2], Clara S. Chan[3], Aaron Thompson[4], Jeffrey G. Catalano[1,5*]

1. Department of Earth and Planetary Sciences, Washington University, Saint Louis, MO 63130, USA

2. School of Marine Science and Policy, University of Delaware, Newark, DE 19716, USA

3. Department of Earth Sciences, University of Delaware, Newark, DE 19716, USA

4. Department of Crop and Soil Science, University of Georgia, Athens, GA 30602, USA

5. McDonnell Center for the Space Sciences, Washington University, Saint Louis, MO 63130, USA

*Corresponding author: catalano@wustl.edu

Table S1. Media composition.

Component	Concentration (mol L^{-1})
Sodium Bicarbonate	2.000×10^{-2}
Ammonium Chloride	1.870×10^{-2}
Calcium Chloride	1.794×10^{-3}
Magnesium Sulfate	4.179×10^{-4}
Dipotassium Hydrogen Phosphate	2.871×10^{-4}
Sodium Chloride	8.556×10^{-5}
Monopotassium Dihydrogen Phosphate	6.613×10^{-6}
Manganese Sulfate	2.958×10^{-6}
EDTA	1.711×10^{-6}
Iron(II) Sulfate	3.597×10^{-7}
Zinc Sulfate	3.477×10^{-7}
Cobalt(II) Nitrate	3.436×10^{-7}
Boric Acid	1.617×10^{-7}
Nickel(II) Chloride	8.414×10^{-8}
Pyridoxine Hydrochloride	4.863×10^{-8}
Sodium Molybdate	4.133×10^{-8}
Nicotinic Acid	4.061×10^{-8}
Copper Sulfate	4.005×10^{-8}
Potassium Aluminum Sulfate	3.873×10^{-8}
Disodium Tungstate	3.032×10^{-8}
Thioctic acid	2.424×10^{-8}
Thiamine	1.884×10^{-8}
p-Aminobenzoic Acid	1.588×10^{-8}
Riboflavin	1.328×10^{-8}
Calcium Pantothenate	1.049×10^{-8}
Biotin	8.186×10^{-9}
Disodium Selenite	5.782×10^{-9}
Folic Acid	4.531×10^{-9}
Vitamin B12	3.689×10^{-9}

Section S1: Local Coordination Environment of Iron in Synthetic Smectites

The EXAFS spectra (**Fig. S1**) of the synthetic smectites are similar to previously-published spectra of smectites with similar composition (Chemtob et al., 2015). The two primary features in the Fourier transform at ~1.7 and ~2.8 Å correspond to the oxygen coordination shell and neighboring octahedral and tetrahedral cations, respectively. The first feature is well-modeled (**Table S2**) with a shell consisting of a mixture of oxygen atoms in octahedral coordination distributed between a longer Fe(II)-O distance (~2.1 Å) and a shorted Fe(III)-O distance (~1.9 Å). The contribution from the oxygen shell around Fe(III) is poorly constrained because of its low abundance. The second feature is a composite of the contributions of octahedral Fe, Mg, and Al neighbors as well as Si in the tetrahedral sheet. The overlap and phase differences among these atoms prevents independent quantification of their structural parameters. A constrained model, as described in the methods section, consisting of each atom with a coordination number determined from the clay composition (**Table S2**) reproduces the data. The interatomic distances are consistent with those expected for Fe(II)-bearing trioctahedral smectites (Chemtob et al., 2015). The ability to model the spectra using a random distribution of octahedral cation neighbors suggests that Fe(II) does not preferentially partition into only cis or trans sites in the octahedral sheet.

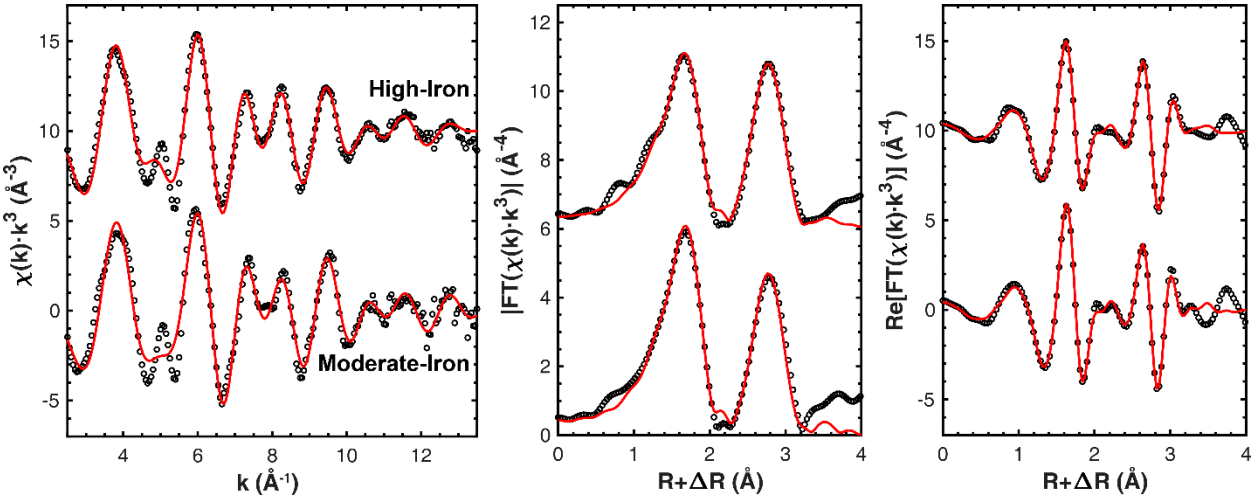

Figure S1. Data (dotted) and structure model fits (solid) to the Fe K-edge EXAFS spectra (left), Fourier transform magnitudes (center), real components of the Fourier transform (right) of the moderate- and high-iron synthetic trioctahedral smectites.

Table S2. Fe K-edge EXAFS fitting results.

Sample	Path	N[a]	R (Å)[b]	σ^2 (Å^2)[c]	ΔE_0 (eV)[d]	R-factor[e]	χ_ν^2 [e]
Moderate-Iron							
Initial	Fe^{II}-O	5.64	2.10(2)[f]	0.009(2)	-4(3)	0.045	135
	Fe^{III}-O	0.36	1.9(1)	0.006(1)			
	Fe-Fe	3.42	3.08(4)	0.009(2)			
	Fe-Al	0.66	3.08	0.004(4)			
	Fe-Mg	1.56	3.08	0.004			
	Fe-Si	4	3.30(7)	0.015(9)			
21% O_2	Fe^{II}-O	1.56	2.12(4)	0.009(4)	-3(2)	0.013	150
	Fe^{III}-O	4.44	1.98(1)	0.012(2)			
	Fe-Fe	3.42	3.04(3)	0.016(5)			
	Fe-Al	0.66	3.04	0.006(2)			
	Fe-Mg	1.56	3.04	0.006			
	Fe-Si	4	3.24(4)	0.014(4)			
H_2O_2	Fe^{II}-O	0.36	2.16(8)	0.009(10)	-5(2)	0.008	57.4
	Fe^{III}-O	5.64	1.97(1)	0.013(1)			
	Fe-Fe	3.42	3.00(3)	0.019(6)			
	Fe-Al	0.66	3.00	0.008(2)			
	Fe-Mg	1.56	3.00	0.008			
	Fe-Si	4	3.21(4)	0.019(4)			
High-Iron							
Initial	Fe^{II}-O	5.52	2.09(1)	0.010(1)	-4(2)	0.028	189
	Fe^{III}-O	0.48	1.88(5)	0.007(7)			
	Fe-Fe	4.70	3.12(4)	0.011(3)			
	Fe-Al	0.48	3.12	0.005(11)			
	Fe-Mg	0.52	3.12	0.005			
	Fe-Si	4	3.28(5)	0.014(1)			
21% O_2	Fe^{II}-O	0.85	2.12	0.010	-4(1)	0.013	170
	Fe^{III}-O	5.15	1.98(1)	0.010(1)			
	Fe-Fe	4.70	3.04(2)	0.013(1)			
	Fe-Al	0.48	3.04	0.002(1)			
	Fe-Mg	0.52	3.04	0.002			
	Fe-Si	4	3.18(4)	0.022(9)			
H_2O_2	Fe^{II}-O	0.30	2.12	0.011	-4(1)	0.015	244
	Fe^{III}-O	5.70	1.97(1)	0.011(1)			
	Fe-Fe	4.70	3.02(2)	0.013(1)			
	Fe-Al	0.48	3.02	0.001(1)			
	Fe-Mg	0.52	3.02	0.001			
	Fe-Si	4	3.14(4)	0.023(9)			

[a] Coordination number. [b] Interatomic distance. [c] Debye-Waller factor. [d] Difference in the threshold Fermi level between the data and theory. [e] Goodness-of-fit parameters (Kelly et al., 2008). [f] The estimated standard deviations are listed in parentheses, representing the uncertainty in the last digit. Parameters with no listed uncertainties were not varied in the analyses.

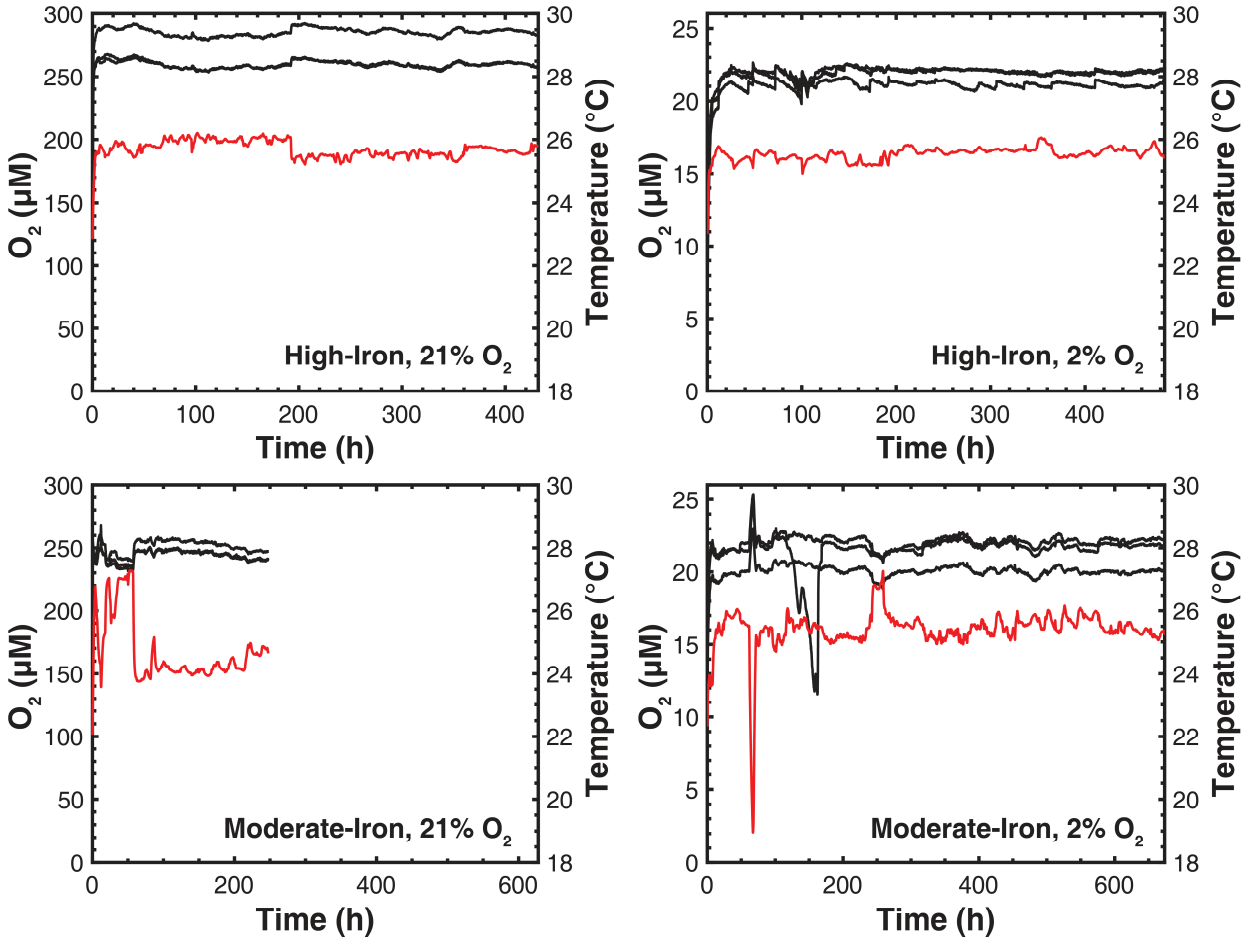

Figure S2. Dissolved oxygen and temperature measurements for the oxygen-equilibrated experiments. The black lines represent the measured oxygen concentration in each of the triplicate reactors. The singular temperature measurement is in red. A computer malfunction terminated data collection early after 250 h for the moderate-iron, 21% O_2 study. Note that the moderate-iron, 2% O_2 experiment experienced two deviations that did not perceptibly affects the results of the study. First, a building heating problem occurred between 62 and 72 h into the experiment, which appears as a transient 6°C decrease in temperature and a correspond slight increase in dissolve O_2 concentration. Second, the gas line to one reactor developed a clog at ~120 h that was corrected 40 h later, with a partial drawdown in dissolved O_2 concentration in the intervening time. This reactor showed no detectable difference in the extent of Fe(II) oxidation compared to the other two reactors after this event.

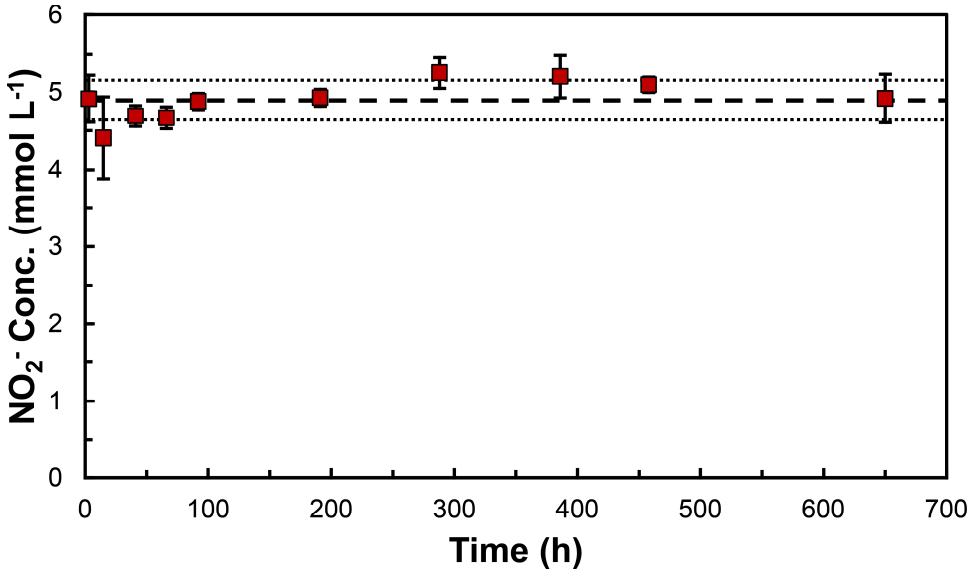

Figure S3. Dissolved nitrite concentrations during reaction with the moderate-iron smectite, reported as the mean and standard deviation of analyses of the triplicate reactors. The dashed lines show the average nitrite concentration over the course of the experiment as well as plus or minus one standard deviation of the nitrite concentration.

Section S2: Rate Equation for the Fitting of Control and Nitrite Exposed Smectites

The single site, pseudo-first order model used to fit the control and nitrite exposed smectite datasets follows a rate defined by equation A.1:

$$\frac{d[Fe(II)]}{dt} = ka_1 \quad \text{(A.1)}$$

Where k is the rate constant, and a_1 is the portion of Fe(II) governed by that rate. The integrated rate equation (Equation A.2) additionally incorporates a nonreactive portion, a_2:

$$Fe(II)_t = a_1 e^{-kt} + a_2 \quad \text{(A.2)}$$

The integrated rate equation was fit to each dataset in MATLAB using a Levenberg-Marquardt nonlinear least squares regression with each datapoint weighted by the experimental uncertainty in that point.

Table S3. Fitting parameters for the oxidant free control and nitrite exposed samples.

Smectite	Oxidant	k (h^{-1})[a]	a_1	Nonreactive Fe(II) Fraction (a_2)	Reduced χ^2
Moderate-Iron					
	None	0.00±0.02[a]	0±100	1±100	1.008
	NO_2^-	0.003±0.006	0.07±0.05	0.82±0.06	4.001
High-Iron					
	None	0.0±0.4	0.00±0.03	0.91±0.02	0.509
	NO_2^-	0.0009±0.0008	0.1±0.2	0.7±0.1	0.268

[a] k is the rate constant fit to the pseudo-first order kinetics and a_1 is the portion of ferrous iron controlled by that rate. The recalictrant portion is the portion determined by the model to be non-reactive.

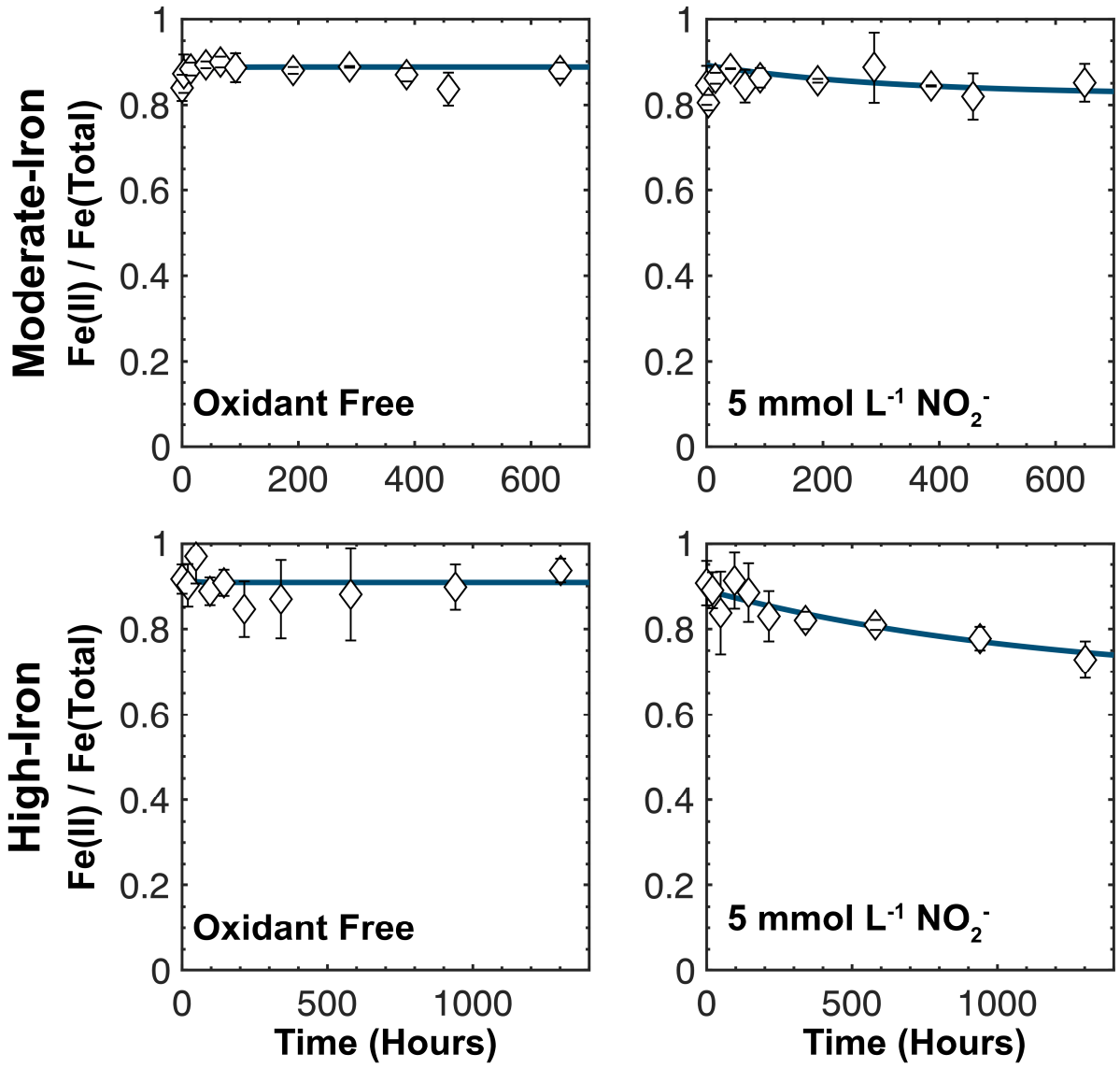

Figure S4. Fe(II)/Fe(Total) and modeled rates of oxidation for both smectite compositions (rows) for both oxidant-free controls (left) and 5 mmol L^{-1} NO_2^- (right). Open diamonds are the datapoints, with errors on each point. Solid lines are the pseudo-first order fit.

References

Chemtob, S.M., Nickerson, R.D., Morris, R.V., Agresti, D.G., Catalano, J.G., 2015. Synthesis and structural characterization of ferrous trioctahedral smectites: Implications for clay mineral genesis and detectability on Mars. J. Geophys. Res.: Planets 120, 1119-1140.

Kelly, S.D., Hesterberg, D., Ravel, B., 2008. Analysis of Soils and Minerals Using X-ray Absorption Spectroscopy, Methods of Soil Analysis Part 5—Mineralogical Methods. pp. 387-463.